

Reply to reviewer 1

We greatly appreciate the reviewer's invaluable and constructive comments. We have revised our manuscript in response to your and the other reviewer's comments. Responses to each of the major and minor comments are written below.

1. Major comments

> My first major concern is on the way, the methodology of the "weighted low PV area" is introduced and motivated. While the PV-area conservation equation (Equ. 1) is widely used, the low PV area weighted by the thickness (isentropic density sigma) is introduced in this study (at least to my knowledge). First of all, the weighted low PV area ( $\hat{A}$ ) should be properly defined.

As you suggested, we have added the definition of the PV area to the main text as follows.

$$\hat{A} \equiv \int_{q \leq q_0} \sigma dA = \int_{\lambda} \int_{\phi} \sigma r^2 \cos \phi d\lambda d\phi$$

> Most importantly, I would like to see the derivation of the equation for the weighted low PV area  $\hat{A}$ , i.e. Equ. (3) in the paper.

> Moreover, the derivation of the equation for only the western part of the PV area (Equ. (4)) could also be explained better, e.g. to elucidate the emergence of the Flux term.

> Is the diabatic term (term 2 on right hand side of Equ. (4)) indeed integrated over the whole low PV area, or only over the western part, as I would assume? If sou, please modify the equation to make this clear.

We also agree that Eqs. 3 and 4 need proper derivation, as also suggested by the other reviewer. In addition, as the other reviewer pointed out, the equation for unweighted low PV area, Eq.1, was not properly described in the original manuscript. The multiplicative factor for line element ( $|\nabla_{\theta} q|^{-1}$ ) was missing, while it was properly described in the reference article (Garny and Randel, 2013). Eqs. 3 and 4 need to be revised in a similar way. Moreover, we have noticed that both of those equations have another missing term regarding diabatic heating. We are sorry for the inaccurate description of the original manuscript. The correct forms of Eqs. 3 and 4 are as follows. The derivation of Eqs. 3 and 4 has been added to Appendix B of the revised manuscript and also at the bottom of this reply.

$$\frac{d}{dt} \hat{A}_{\text{tot}}(t) = \oint_{q=q_0} \left( -q \frac{\partial \dot{\theta}}{\partial \theta} + \dot{\theta} \frac{\partial q}{\partial \theta} \right) \frac{\sigma dS}{|\nabla_{\theta} q|} - \int_{q \leq q_0} \frac{\partial}{\partial \theta} (\sigma \dot{\theta}) dA + (\text{unresolved term})$$

$$\begin{aligned} \frac{d}{dt} \hat{A}_{\text{west}}(t) = & -\hat{F}(\lambda_0) + \int_{q=q_0, \lambda \leq \lambda_0} \left( -q \frac{\partial \dot{\theta}}{\partial \theta} + \dot{\theta} \frac{\partial q}{\partial \theta} \right) \frac{\sigma dS}{|\nabla_{\theta} q|} - \int_{q \leq q_0, \lambda \leq \lambda_0} \frac{\partial}{\partial \theta} (\sigma \dot{\theta}) dA \\ & + (\text{unresolved term}) \end{aligned}$$

> Next to the proper definition and derivation, I would appreciate a deeper physical reasoning for the weighting of the PV area. If I understand it correctly, the relevant effect here is that, given the conservation of PV for a given air mass, a vertical (i.e. in theta) compression of this air mass leads to a larger horizontal extend, i.e. an increase in area. Thus, by applying this scaling you essentially move to an equivalent 2-d representation of the air parcel, and  $\hat{A}$  is the area of this equivalent 2-d air parcel. Maybe the addition of a simple sketch would help the reader to get a better understanding of the meaning of the scaling.

We appreciate the suggestion. As you pointed out, the weighting of the PV area is related to tracking an air parcel on 2-d surface. We have added the explanation about it at lines 151-160 in Section 2 of the revised manuscript.

> A related question on the scaled versus non-scaled PV area: according to your equations, the divergence term vanishes for the density-scaled area equation. If my above understanding of the weighted-PV area is correct, this would imply, that the role of the divergence term merely is to deform the air parcel. However, as you mention, in earlier work it was shown that the divergence term in the conventional PV area equation is closely related to the diabatic term, and indeed maximizes in the regions of low OLR (as indication for convection). Following this finding, the interpretation would be that the divergence (i.e., convective outflow) induces the low PV, and not merely deforms the air parcel. Is this effect completely incorporated in the diabatic term in the weighted low PV equation, or how can I understand the physical meaning of the terms?

It is the diabatic term that induces low PV, not directly the divergent term. The divergent term is likely to follow the diabatic forcing by deep convection, resulting in high correlation between it and low OLR, but the divergent term without nonconservative forcing does have nothing to do with the weighted low PV area. The revision we made in lines 151-160 in Section 2 in the revised manuscript includes this explanation.

> The period of the “quasi-biweekly” oscillation is not clearly quantified until rather late in

the paper, namely with the power spectrum in Fig. 6. Rather, the motivation for those time-scales is given by visual analysis of the timeseries of the weighted low PV area in Fig. 2. I'd encourage the authors to move the power spectrum to an earlier point in the paper, and compare it to the power spectrum of the total weighted low PV area (see also specific comment below). Further, the peak in the power spectrum of the fluxes (Fig. 6) is rather broad (with a plateau-like peak between 20 to 9 days), does this range of time-scales still correspond to the "quasi-biweekly" oscillation?

We did not mean to state that "quasi-biweekly" timescale is dominant here yet. Rather, section 3.1 exemplifies that the total weighted PV area  $\hat{A}_{tot}(t)$  shows over-30 day variability dominates as already mentioned in earlier studies and there are also secondary signals with a shorter time scale. In this sense, we consider the sentence 'The analysis regarding the total area so far confirmed ...' was misleading. We have revised the first paragraph of section 3.2 to make it clear.

Also, we agree that the peak in Fig. 6 does not show clear characteristic time scale of 'quasi-biweekly'. There is broad range of possible characteristic time scale centered around quasi-biweekly. We have revised lines 226-228 in the revised manuscript.

My third major comment is on the interpretation of the results, mainly the overarching question of the nature of the quasi-biweekly oscillation as "passive advection" versus reflecting variability in sources (i.e., convective forcing) or sinks (e.g., the actual shedding of air from the anticyclone). This comes down to the question, whether the total low PV area is conserved during the oscillations (as is shown for the life cycle analysis in Fig. 13), or, whether the total flux across the defined boundary at 60 E explains the in- and decrease of low PV area to the west and east of the boundary. The latter is indicated to be the case by the close match of timeseries of area change and fluxes in Fig. 5. However, I wonder whether this analysis couldn't be made more quantitative by repeating it for longer time series (multiple years), and actually quantifying to which degree the total western PV area is explained by the flux (for both increasing and decreasing areas, i.e., positive versus negative values of  $d\hat{A}/dt$  and the flux  $F$ ). Also, I wonder to which degree the eastern part of low PV area is explained by the flux term. As the diabatic source is located east of 60 E, it maybe not surprising that the western part is explained by the fluxes from the east. In general, also the location of the boundary at 60 E could be varied to test the sensitivity of the results on the choice of the boundary longitude.

We have found that the close relationship between the flux term  $F$  and the low PV area to the west of 60E is satisfied in general, also for other years. We have shown the correlation factor 0.663 between  $d\hat{A}/dt$  and the flux  $F$  for 1979-2016 in line 204 of the original manuscript.

We consider this value shows that the correspondence between these two terms is quite significant. We do not expect the similar clear relationship for the eastern part of the anticyclone, where the diabatic forcing term has a significant role.

Moreover, the results mentioned above are all valid for the 370 K level (if I'm not mistaken, I found it hard to identify which level the analysis is performed on at many places, see specific comment below). According to your Fig.3, in which the fluxes of low PV area across the 60 E line are shown for both 370 K and 360 K, the fluxes behave rather different at the two levels: At 370 K, the flux is close to zero in the mean (indicating back and forth advection), while at 360 K, the flux is clearly eastward, which is in accordance with the "source" of low PV (i.e. convection) being mostly located east of 60E. Therefore, I wonder in how far the result on the "passive advection" of low PV air is valid also for the 360 K level (which does not lie well above the main convective outflow and heating level, as does the 370 K level).

We have revised Figs. 4 and 5 to show the results at three different levels 360, 370, and 380 K. As expected, the contribution of the longitudinal advection to the low PV area distribution is less clear at 360 K at 380K, as there are more significant source and sinks. The whole picture of the budget of low PV air mass is more complicated than what is seen at a single level, we consider the longitudinal oscillatory behavior with a time scale of quasi-biweekly is one important feature, and the low PV air at 370 K is the best proxy for that feature. We have revised section 3.2 adding this discussion.

Another major comment I have is on the interpretation of the OLR anomalies during the oscillation life cycle (as presented in Fig. 14). I can identify from the figure a clear signal in the OLR anomalies, with westward propagating negative OLR anomalies during phase 5 to 8, and positive OLR anomalies during phase 2 to 4. Thus, this might suggest that variability in the forcing of the anticyclone does play a role on those time-scales after all. This possibility is indeed phrased in the summary (lines 329-330), but this is a bit controversial to what is stated earlier (e.g. lines 302 to 303). On the other hand, the consistent OLR anomalies could also indicate that the quasi-periodic circulation anomalies of the anticyclone influence the occurrence of convection. This result might be consistent with the troposphere-deep circulation anomalies at 35-45 N, as shown in Fig. 15. This possible implication is discussed in the summary (lines 335 onwards), but I'd suggest that you could add here, that the OLR anomalies in the "life cycle" also show indications in this direction.

We consider the existence of the significant OLR signal does not rule out the possibility that the variability is driven by internal dynamics, then lines 329-330 and 302-303 of the original manuscript does not contradict with each other. The OLR anomaly in composite map can be

just a response to the dynamically-driven variability as well as the essential driver of the variability. We does not conclude it but provide the suggestion of the possibility of the former case, considering the spatial location of OLR anomaly and low PV area in phase 6. This has been written in lines 324-330 in the original manuscript but the explanation may be not clear. We have revised lines 276-278 in Section 4 and a paragraph starting from line 336 in Section 5 in the revised manuscript.

## 2 Specific / minor comments

- title: Change to “geopotential height fields”. In my opinion, the latter half of the title (“.. using PV and geopotential...”) could also be skipped, but this is a matter of taste, so I leave it to the authors to decide.

We appreciate the suggestion. We have added ‘height’ to the original title.

- line 24: ”to be dominant“: consider rephrasing to ”to be the dominant transport process“  
We have revised line 24 as suggested.

- line 48-50: I wouldn’t agree in that the paper by Nuetzel et al showed that the bimodality is a robust feature. Indeed, they showed that the bi-modality is very prominent only in older (NCEP) reanalysis data sets.

We appreciate the important comment. Our original manuscript does not correctly refer to their conclusion. We have revised lines 47-49 in the revised manuscript.

- line 113: This sentence makes it sound as if the low PV area in the anticyclone is usually conserved, but just not strictly, because of the ”forcing processes such as deep convection“. Diabatic heating and associated outflow from deep convection (divergent motion) is THE forcing process of the anticyclone, if it wasn’t for that, there would be no low PV area to start off with. Therefore, I find this formulation a little weird. Please rephrase it to make the role of deep convection on forcing low PV more clear.

We meant to emphasize the effect of thickness variation as another factor which causes the change in the low PV area, besides of the diabatic heating. We have revised lines 110-113 of the revised manuscript to provide clearer explanation.

- line 130 / Equ. 2: On a similar note as major comment 1, a definition for the longitude-dependent quantity  $L(\lambda, t)$  along the lines suggested for  $\hat{A}$  could be given (i.e. as integral over  $\phi$ ).

We have added Eq. (4) for the definition.

- line 171: here, the authors state that the analysis of the timeseries in the preceding subsection ”confirmed” that the dominant timescale of variability is the ”quasi-biweekly”

timescale. However, in the daily timeseries presented in Fig. 2, a monthly period is predominant, and the quasi-biweekly timescale is, if at all, only to be guessed "by eye". So either you have to weaken the statement here (e.g. indicates that quasi-biweekly variability can be identified from the timeseries) or make the analysis more quantitative (see also major comment 2).

We agree the statement 'The analysis regarding the total area so far confirmed ...' was too strong. It was not confirmed in the previous section. We have revised the first paragraph of section 3.2.

- line 186: For 360 K, the flux is negative around its minimum, even within the range given by the standard deviation. So this argument holds only for Fig 3a (370 K), right?

We think it is still possible for the airmass to move both eastward and westward even the latitudinally averaged flux is mostly westward at 360K. But in that situation, the interpretation is more complex because the movement of passive tracer does not follow the movement of the airmass as there is a large nonzero PV source/sink. Therefore, we limit this statement only for 370K and 380K where the diabatic process is less significant. We have revised section 3.2 accordingly.

- line 193/194: "fixed latitude range in the southern part of the AMA" - in Garny et al, the total low PV area within 15-45 N was shown (see their Fig. 6), so this is not really a fixed latitude range, and neither only the southern part? The main difference is, apart from the slightly larger latitude range here, rather the weighted versus non-weighted low PV area, and the addition of the fluxes.

We agree that the statement was not accurate. The difference from Garny et al. is basically the thickness weighting that may give clearer picture to focus on both westward and eastward movement of the air. We have revised the description in line 205-207 of the revised manuscript.

- line 197: why only "as far as PV conservation holds"? Is the flux not valid if the the diabatic term is not equal zero? This would be worrisome for the whole analysis of the paper.

We meant that the interpretation using the simple relationship between the low PV air mass and its flux is valid under the assumption of the PV conservation. However, it is true that we can use the flux itself regardless of the conervation as you suggested. We have simply removed the phrase 'as far as PV conservation holds'.

- line 209: "dominant period of the variability in total low PV area" - actually show the power spectrum of the low PV area (see also comment on line 171, and major comment

2)?

The dominant period of the variability seen in the total low PV area has been found to be around 30 days in previous studies, and we do not mean to revisit it. We should have put the reference Garny and Randel (2013) here. We have added the reference, and revised the paragraph following your major comment.

- line 219: Do you mean to say that the timeseries filtered with a band pass filter within 5-20 days periods? Please specify.

Yes, that is what we did. We have added the description to the first paragraph of Section 4.1.

- line 232: "zonally averaged total perturbation variance": Do you mean the variance in terms of anomalies at each longitude, and then this variance is zonally averaged?

Yes we do. The original manuscript meant to describe the contribution of the leading two components to the total variance as a function of latitude. However, we reconsider that this statement is not necessary and decided to remove.

- line 233: the studies mentioned here rather analyzed tele-connections to the mid-latitudes than variability of the anticyclone itself, correct? So maybe it is not surprising that they find different pattern? ( Also, correlation to the time-series "at a point at a midlatitude" is a bit vague - please clarify).

Yes. As they focus on midlatitude dynamical variability they used different methods and target variables and captured different variability patterns.

In this part, it was found that the description "simple correlations with a time series at a point at a midlatitude" was not correctly described what has been done in Ding and Wang (2007). They made the composite analysis for the extreme events of positive geopotential height anomaly averaged over 35-45°N,55-75°E. We are sorry for misleading. We have revised line 250-251 of the revised manuscript accordingly.

- I find the EOF analysis, and the PC lag analysis and life cycle a great approach to characterize the variability. Possibly, adding actual data points to Figure 9 to see the progression of the phases would be beneficial?

We appreciate the suggestion. The phase progress for the year 2016 has been added to Fig 9 as an example. Also, the caption of Fig. 9 has been revised.

- Fig. 11: agree that there is clear westward extension from phase 5 to 8, but does the low PV area "move back" to the east from phase 1 to 4, or is it shed? From the extend and strength of the low PV occurrence, it seems like the total PV area decrease over those phases. Related, is the total integral over the westward flux (in Fig. 12) equal to the sum of the eastward Flux over all phases? This would prove this point, and I guess it has to

be the case, given that the total area appears to remain rather constant according to Fig. 13.

Our idea based on Figs. 12 and 13 is that, the low PV area mostly moves back to the east rather than 'shed' westward away from the main anticyclone vortex. Though this does not rule out the existence of some part of low PV actually shed and dissipated to the west, the shedding is likely to have only a small contribution to the budget of the air inside the anticyclone. This is supported by Figs. 12 and 13. The eastward and westward flux is nearly balanced on average over phases and the total PV area is nearly constant with the phase. The fact that the area of high low-PV probability decreases as phase progresses from 1 to 4 in Fig. 11 can be explained by the thickness variation. The average  $\sigma$  over 30°N is larger than that over 20°N on 370 K. Therefore, when the weighted low PV area does not change, the low PV airmass takes smaller area when it is moved northward in phase 2-4.

- Fig. 15: Not sure what the difference of black contours and color shading is - deviations from zonal mean versus anomalies from this deviation?

The black contours show the deviation from the longitudinal mean over the sector (0-150E) for each phase, which indicates the location of the anticyclone center. It shows how the variability is large enough to change the anticyclone location

The color shading shows the deviation from climatological mean, which indicates the longitudinal structure of the perturbation.

- lines 281-282: I'm not sure I understand the statement on the role of the subtropical jet on the deep gph anomalies. Please either remove, or add explanation/ citation for this statement.

What determines the vertical structure of the variability pattern is beyond the scope of this article. Therefore we have removed that sentence for simplicity.

- line 307: would you consider 30% of variability from both the 1st and 2nd EOF together the "dominant variability"?

We consider the leading two EOF components corresponds to the most significant variability pattern in the area in a 5-20 day time scale. But the word 'dominant' may sound not suitable for the components which contribute to only about 30% of the total (normalized) variance. Therefore we have removed the word "dominant" from the sentence in line 336 of the revised manuscript.

- line 305/306: here you state that the west/east-ward flux of low PV is consistent with "eddy shedding", which could be true, but this notation implies that the eddies are at least partly "shed" from the Anticyclone, while your analysis seems to suggests that the total area is conserved during the quasi-biweekly variability, i.e. no actual "shedding" occurs. In Fig.3 b), where you show that the total eastward flux at 360 K is negative,

does that imply actual westward shedding?

We used the word 'eddy shedding', in lines 252 and 305/306 in the original manuscript, in a broader context describing the westward movement and the detachment of the partial anticyclonic vortex from the main anticyclone, regardless of whether it is reversible or not. But later we stated in line 347 that they are mostly not actual 'shedding' at 370K level as you suggested, This might have made confusion, therefore we revised those lines without the notation 'eddy shedding'.

About the low PV area budget at 360 K, there is still no clear answer from the result of this study. The source of the weighted low PV area on 360K is likely to be diabatic heating over the area of deep convection located over the eastern part of the anticyclone. But its sink on the west of the anticyclone cannot be specified. The westward shedding may contribute, but it may be by diabatic heating/cooling. We have revised section 3.2 and include this discussion to line 217-225.

- general: State in all Figure caption, and possibly more often in the text, at which level the analysis is performed on! (I found this information to be rather hidden).

We are sorry for the insufficient information. We have added proper information of the isentropic and pressure level in the text (in lines 189, 202, 273, and 274) and the figure captions (Figs. 4, 5, 6, 12, 13, and 14).

3 Typos / technical

- line 165: "pointed out by..." (add "out")
- line 220: dividing "by" their standard deviation (insert "by" )
- line 225: "longer months": change to "longer period" ?
- line 275: "rest phases": change to "for the rest of the phases" ?
- Fig. 15: Title and legend should say 15-25N and 35-45N rather than E.
- line 409: "noize": change to "noise"
- line 420: "persentage": change to "percentage"
- Fig. 4: which level?
- Fig. 13: I would suggest to change/remove the heading "A west", as not only "A west" is shown

We have corrected the manuscript accordingly.

Reply to reviewer 2

We greatly appreciate the reviewer's invaluable and constructive comments. We have revised our manuscript following your and the other reviewer's comments. Responses to each of the major and minor comments are written below.

Major comments

> It is unclear whether it is a major or minor point but the basic equation (1) which is taken from Garny and Randel (2013) is technically wrong as it is presented. The integrand  $dS$  in the first member of the r.h.s. is not a line element but a line element divided by the modulus of the horizontal gradient of the PV. This is stated by Garny and Randel and, otherwise, the equation is not even dimensionally homogeneous. I hope that this detail has not been missed by the authors and that the error was only introduced during writing but it is quite worrying. It is true that the factor of a line element was missing in Eqs. 1, 3, and 4. Additionally, we also found another missing term which should be added in the right hand side of Eqs. 3 and 4. Correct forms of those equations are as follows. Their derivations are added to Appendix B of the revised manuscript and also at the bottom of this reply. We are sorry for the incorrect description. This correction does not affect our analysis results in this study, as the integral terms are not directly used.

$$\frac{d}{dt} \hat{A}_{\text{tot}}(t) = \oint_{q=q_0} \left( -q \frac{\partial \dot{\theta}}{\partial \theta} + \dot{\theta} \frac{\partial q}{\partial \theta} \right) \frac{\sigma dS}{|\nabla_{\theta} q|} - \int_{q \leq q_0} \frac{\partial}{\partial \theta} (\sigma \dot{\theta}) dA + (\text{unresolved term})$$

$$\begin{aligned} \frac{d}{dt} \hat{A}_{\text{west}}(t) = & -\hat{F}(\lambda_0) + \int_{q=q_0, \lambda \leq \lambda_0} \left( -q \frac{\partial \dot{\theta}}{\partial \theta} + \dot{\theta} \frac{\partial q}{\partial \theta} \right) \frac{\sigma dS}{|\nabla_{\theta} q|} - \int_{q \leq q_0, \lambda \leq \lambda_0} \frac{\partial}{\partial \theta} (\sigma \dot{\theta}) dA \\ & + (\text{unresolved term}) \end{aligned}$$

The main claim of the manuscript is that the oscillations are mostly of dynamical origin and reversible, and that forcing by convection and dissipation are not involved. This is quite opposite to conclusions of previous works and also to Wei et al. (2019, doi:10.1029/2019GL086180) and references herein which is another stream of research that should be quoted and discussed. Another relevant work that studies PV fluxes on isentropic surfaces is Ortega et al. (2018, doi: 10.1002/qj.3261) which is also missing in the reference and should be used to compare the results of the manuscript.

About the causal relationship between convective forcing (particularly over Indian sector) and

the dynamical variability in the upper troposphere, we do not very much agree with the argument of Wei et al. for two reasons. First, their result that the negative rainfall anomaly over northern India precedes the key day of the anticyclone east-west oscillation may be a consequence of the choice of the key day and the definition of the variability index, a difference between area-averaged GPH over Tibetan Plateau and Iranian Plateau. Second, they did not provide convincing mechanism of convection anomaly over northern India driving the dynamical field anomalies including midlatitudes. They referred to Karmakar et al. (2017), and Ding and Wang (2007), Karmakar et al. did not propose physical process responsible for it. Ding and Wang suggested a mutual positive feedback, in which midlatitude upper level circulation anomalies enhances the convection and in turn the convection triggers the midlatitude Rossby wave train. Thus they do not exclude the possibility that the convection anomaly is forced by the upper level circulation anomalies.

The results of a composite analysis in Wei et al. (their Fig. 3) and ours (Fig. 14) do not necessarily agree for the feature of convection anomalies. The difference may come from the different reference index and the different pressure level. The discussion about this point has been added to the revised manuscript.

We have added the reference to their work in line 350 in discussion section.

The formulation used in Ortega et al. has some similarity to ours, but it used the different definition of flux for the different purpose. They focus on PV value and its thickness-weighted flux in latitudinal direction, whereas our study focuses on the weighted area enclosed by a PV contour, and longitudinal flux of that area (mass). Their definition cannot well quantify the movement of the air inside the anticyclone as the PV-based definition can do. We have added the reference to Ortega et al. (2018) and this explanation in line 156-158 of the revised manuscript.

The manuscript focuses on the zonal mass flux of air with low PV and finds that the mean flux at 370K oscillates around zero over the range of latitudes of the AMA. This is basically the main result. However, this does not mean that there is no zonal flux of PV. It is clear from fig.11 that during the phase of eastward flux at 60E, the air carries less negative PV than during the phase of westward flux. Therefore the zero mean mass flux does not rule out a non zero mean PV flux, where negative PV is created on the east by convection and dispersed and lost to the background on the west by vortex shedding within a biweekly cycle. It is useful to notice that the circulation time around the anticyclone and its erosion rate are also of about two weeks (Legras and Bucci, 2019, doi: 10.5194/acp-2019-1075). PV is clearly not well conserved during the bi-weekly cycle.

We appreciate reminding the important difference between the conservation of the low PV area and the conservation of PV values. The description in the original manuscript which is based on PV conservation is not appropriate in this sense. Our discussion is based on the budget of the weighted low PV area. This view has better implication for the variability of chemical tracers, given that the threshold PV value properly reflects the mixing barrier. We have revised lines 158-160 in the revised manuscript to make this point clear.

#### Minor comments

l. 51-53: Is it so clear that the two questions are well separated?

These two questions can be treated separately, because the intensity and position/structure of the AMA can be quantified independently with each other.

l. 63 “is often”

We have revised the sentence in this line as suggested.

l. 141: I do not see why the divergence term disappears in this equation.

We have added the derivation of Eqs. 3 and 4 in Appendix B in the revised manuscript.

l. 145: The integral is at fixed longitude and the integrand is latitude over the range where the PV is below the threshold and F is the mass flux (rather than the movement) of low PV air across a given latitude. This is badly described and the scheme in fig.1c adds to the confusion.

We have revised lines 148-149 in the revised manuscript as suggested.

l. 164: I do not see the need for a 31-day filter when the average is done over 38 years. This should be enough to scramble the phases of the AMA oscillations.

We used a low-pass filter to ensure that it represents the mean seasonal variation, although it does not change much of the result.

l. 173: At this stage, the evidence is only based on the visual appearance of a single year record.

The statement in line 173 of the original manuscript ‘The analysis regarding the total area so far confirmed ...’ was not appropriate. We have revised the first paragraph of section 3.2.

l. 176: This line should refer to eq. (5) if this is what is shown.

We have added the reference of the equation.

l. 181: This line makes me worrying whether the total heating, including latent heating, is accounted as it should in this work or whether only radiative heating is used. At 370K, it is however correct to assume that radiative heating dominates.

The notation ‘differential radiative heating’ was misleading, as other processes such as latent heating should be accounted as well. We have revised the line 193 of the revised manuscript.

l. 190: I assume that the results are shown on the 370 K surface but this should be stated. It is very difficult to distinguish the blue and red contours in fig. 4. The text mentions that fig. 4 shows the mass weighted length that should have dimension  $\text{kg}/(\text{K} \times \text{m})$  and the caption says that it is a weighted area with dimension  $\text{kg}/\text{K}$ . Please clarify. Provide a definition for this weighted area that depends on the longitude and discard  $L$  if it is not used.

The value shown in Figure 4 has a unit of  $\text{kg}/\text{K}$  and factor of  $10^{12}$ . It is the weighted area calculated over each grid area and summed up for latitudinal direction. We have revised the figure caption and the description in lines 201-202. We also have made blue contours in Fig. 4 thicker and dashed to make them more visible.

In the sequel, no PV diagnostic is shown on other surfaces than 370K. The choice of 370K is justified in the appendix on the basis of the best definition of AMA in terms of PV but it would nevertheless be interesting to look at other surfaces. 380 K was privileged in Ploeger et al. (2015) and 360 K is closer to the level where convective detrainment is the strongest. It is also where the mean eastward and westward branches of the AMA are maximum and where the isentropic divergence is maximum.

We have revised Figs. 4 and 5 to show the results at three different levels 360, 370, and 380 K. As expected, the contribution of the longitudinal advection to the low PV area distribution is less clear at 360 K at 380K, as there are more significant source and sinks. The whole picture of the budget of low PV air mass is more complicated than what is seen at a single level, we consider the longitudinal oscillatory behavior with a time scale of quasi-biweekly is one important feature, and the low PV air at 370 K is the best proxy for that feature. We have added these discussions to section 3.2 of the revised manuscript.

l. 197: I do not see why PV conservation is invoked here. It is clear that PV is not well conserved here (see fig.11).

As the other reviewer also pointed out, the PV conservation needs not be assumed here for the use of the longitudinal flux of the low PV area. We have removed that phrase from the original manuscript.

l. 209 and Fig. 6: How should we interpret the significance curves on Fig. 6? The peak is not that strong and shows there is a plateau in the spectrum intensity between 9 days and 25 days. 9 days is more a cutoff period than a dominating period.

We agree that the peak in Fig. 6 does not show clear characteristic time scale of 'quasi-biweekly'. There is a broad range of possible characteristic time scale centered around quasi-biweekly. We have revised lines 226-228 in the revised manuscript.

Sect. 4 It is a bit surprising that the study switches here to the geopotential on the 100 hPa surface. Having done all the work to interpolate basic variables on isentropic surfaces would have made easy to calculate the Montgomery potential on such surfaces. Basically, the results would not have been very different but this would have been more consistent, especially because isentropic and isobaric surfaces may differ quite significantly in the Asian monsoon region. As the authors are looking for a cycle, they should have considered the MSSA method which is particularly well suited (Ghil et al, 2012, doi:10.1029/2001RG000092) and would have saved time and space.

The use of Montgomery potential may be consistent in our analysis. However, we rather chose geopotential at the 100 hPa pressure surface for the EOF analysis in order to make the comparison with earlier studies easier, as most studies on the bimodality of the AMA center location used 100 hPa geopotential height. The result would be similar if we perform the analysis using Montgomery streamfunction on 380 or 390 K level.

The extended EOF analysis is mathematically equivalent to MSSA (Plaut and Vautard, 1994) and more often used in geophysical studies in which the number of spatial grid points are much larger than the number of time steps in a cycle. For example, Wang and Duan (2015) used extended EOF for 10-20 day filtered diabatic heating in the Asian monsoon region.

We did extended EOF and complex EOF analyses and got the similar results to the case of EOF analysis, as mentioned in line 225 in the original manuscript. We only show the result of EOF analysis for simplicity.

#### 1. 220 “dividing by their”

We have revised the sentence in line 236 in the revised manuscript as suggested.

#### 1.220 Why the square root of grid area and not the area in the weight?

When the data is weighted by the area, the variance or correlation should be multiplied by the area. This corresponds to multiplying the anomaly by the square root of the area.

1. 240: It is quite difficult to understand fig. 9 which is introduced in a section where PV plays no role. Please improve the caption such that it makes sense when the reader is at line 240 in the text.

The caption of Fig.9 was incorrectly input. We are very sorry for the mistake. We have replaced it with the correct caption.

Sect. 4.2 The first paragraph concludes that variability is determined by internal inviscid and adiabatic dynamics but the second paragraph shows there is a pattern of convection associated with the oscillation which somewhat contradicts the first paragraph if we admit that convection does not only react passively but generates a forcing. The authors do not attempt to provide a balanced view and just discard the convective influence in this section and in the

[conclusions 1.323-330.](#)

About the role of the convection variability, we does not conclude but suggest the possibility that the dynamical variability drives the convection variabilty, considering the spatial location of OLR anomaly and low PV area in phase 6. This has been written in lines 324-330 in the original manuscript but the explanation may not be clear. We have revised lines 276-278 in Section 4 and a paragraph starting from line 336 in Section 5 in the revised manuscript.

(derivation of Eqs. 3 and 4)

Equation 3 can be derived in a way similar to the derivation of Eq. (13) of Butchart and Ramsberg (1986). For consistency, their notation is used in the following.

They begin with the small change in the area  $\Delta A(t)_{\chi \geq \chi_0}$  as a function of  $\Delta \mathbf{x}$ . Note that they assumed that the value of  $\chi$  increases inward of the area.

$$-\oint_{\Gamma} \Delta \mathbf{x} \cdot \frac{\nabla_{\theta} \chi}{|\nabla_{\theta} \chi|} ds = \Delta A(t)_{\chi \geq \chi_0}$$

To extend this formulation to the thickness-weighted area  $\Delta \hat{A}(t)_{\chi \geq \chi_0}$ , there needs an additional term for thickness change  $\Delta \sigma$ .

$$\int_{\chi \geq \chi_0} \Delta \sigma dA - \oint_{\Gamma} \Delta \mathbf{x} \cdot \frac{\nabla_{\theta} \chi}{|\nabla_{\theta} \chi|} \sigma ds = \Delta \hat{A}(t)_{\chi \geq \chi_0}$$

Using the basic equation for thickness

$$\frac{\partial \sigma}{\partial t} + \nabla_{\theta} \cdot (\sigma \mathbf{v}) = -\frac{\partial}{\partial \theta} (\sigma \dot{\theta}),$$

the first term on the left hand side can be rewritten as follows.

$$\begin{aligned} \int_{\chi \geq \chi_0} \Delta \sigma dA &= \Delta t \left[ -\int_{\chi \geq \chi_0} \nabla_{\theta} \cdot (\sigma \mathbf{v}) dA - \int_{\chi \geq \chi_0} \frac{\partial}{\partial \theta} (\sigma \dot{\theta}) dA \right] \\ &= \Delta t \left[ \oint_{\Gamma} \mathbf{v} \cdot \frac{\nabla_{\theta} \chi}{|\nabla_{\theta} \chi|} \sigma ds - \int_{\chi \geq \chi_0} \frac{\partial}{\partial \theta} (\sigma \dot{\theta}) dA \right], \end{aligned}$$

where  $\mathbf{v}$  is two-dimensional velocity, and  $\nabla_{\theta}$  is two-dimensional gradient on an isentropic surface.

The second term on the right hand side is transformed using  $\Delta \mathbf{x} \cdot \nabla_{\theta} \chi \simeq -\Delta t \partial \chi / \partial t$  as shown in Butchart and Ramsberg (1986). Then by applying  $\Delta t \rightarrow dt$  we obtain the following,

$$\frac{d}{dt} \hat{A}(t)_{\chi \geq \chi_0} = \oint_{\Gamma} \left( \frac{\partial \chi}{\partial t} + \mathbf{v} \cdot \nabla_{\theta} \chi \right) \frac{\sigma ds}{|\nabla_{\theta} \chi|} - \int_{\chi \geq \chi_0} \frac{\partial}{\partial \theta} (\sigma \dot{\theta}) dA$$

As the first integral contains an advection term, the bracket in it can be replaced with a nonconservation term  $F$ .

$$\frac{\partial \chi}{\partial t} + \mathbf{v} \cdot \nabla_{\theta} \chi = F$$

When  $\chi$  is potential vorticity and the area  $A$  is defined to have potential vorticity below the reference value, Eq. (3) is obtained.

The subgrid scale mixing term in Butchart and Ramsberg (1986) comes from the difference between the true divergence term and the divergence term calculated from resolved variables. Although our equation does not have divergence term, we consider it is still better to include unresolved effect such as subgrid scale mixing, which is included in  $F$ . Then, when  $\chi$  is

potential vorticity and the area  $A$  is defined to have potential vorticity below the reference value,

$$F = -q \frac{\partial \dot{\theta}}{\partial \theta} + \dot{\theta} \frac{\partial q}{\partial \theta} + (\text{unresolved term})$$

and we obtain the equation (3).

Equation (3) can also be derived from the general mass conservation expression in a PV-theta coordinate introduced in Nakamura (1995);

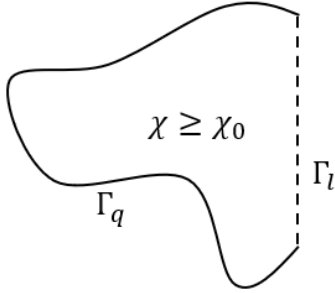
$$\left(\frac{\partial m}{\partial t}\right)_{q,\theta} + \left(\frac{\partial \mathcal{M}(\dot{q})}{\partial q}\right)_{\theta,t} + \left(\frac{\partial \mathcal{M}(\dot{\theta})}{\partial \theta}\right)_{q,t} = 0$$

where  $m = \mathcal{M}(1)$  and thickness-weighted area integration operator  $\mathcal{M}$  is defined as

$$\mathcal{M}(\ast) = \int \int_{q \leq q_0} (\ast) \sigma dA = \int_{q^\ast \leq q} dq^\ast \oint_{q^\ast} (\ast) \frac{\sigma ds}{|\nabla_\theta q^\ast|}$$

Substituting the expressions  $\mathcal{M}(\dot{q})$  and  $\mathcal{M}(\dot{\theta})$  to ( ) and  $\dot{q} = F$  in ( ), we obtain Eq.3.

(derivation of Eq.4)



Now suppose the small change of the area  $\Delta \hat{A}(t)_{\chi \geq \chi_0, \lambda_0}$  enclosed by the isopleth  $\chi \geq \chi_0$  and the circle of longitude  $\lambda_0$ . Let  $\Gamma_q$  and  $\Gamma_l$  respectively be the isopleth and the circle of longitude consisting the border of the area. The equation for  $\Delta \hat{A}(t)_{\chi \geq \chi_0, \lambda_0}$  is modified as follows.

$$\int_{\chi \geq \chi_0} \Delta \sigma dA - \oint_{\Gamma_q} \Delta \mathbf{x} \cdot \frac{\nabla_\theta \chi}{|\nabla_\theta \chi|} \sigma ds = \Delta \hat{A}(t)_{\chi \geq \chi_0, \lambda_0}$$

The integral of the first term on the left hand side is performed over the area  $\Delta \hat{A}(t)_{\chi \geq \chi_0, \lambda_0}$ , and the line integral of the second term is performed only over  $\Gamma_q$ , as  $\Gamma_l$  is constant with time.

The first term can be rewritten as follows, using the Gauss' theorem for  $\Gamma_q$  and  $\Gamma_l$ .

$$\int_{\chi \geq \chi_0} \Delta \sigma dA = \Delta t \left[ - \int_{\chi \geq \chi_0} \nabla_\theta \cdot (\sigma \mathbf{v}) dA - \int_{\chi \geq \chi_0} \frac{\partial}{\partial \theta} (\sigma \dot{\theta}) dA \right]$$

$$= \Delta t \left[ \int_{\Gamma_q} \mathbf{v} \cdot \frac{\nabla_{\theta} \chi}{|\nabla_{\theta} \chi|} \sigma ds + \int_{\Gamma_l} u \sigma ds - \int_{\chi \geq \chi_0} \frac{\partial}{\partial \theta} (\sigma \dot{\theta}) dA \right]$$

Then we obtain Eq. 4 with the additional term  $\hat{F}(\lambda_0)$  defined as follows. The integral is performed over the longitude circle  $\lambda_0$  consisting the border of the area.

$$\hat{F}(\lambda_0) = \int_{q \leq q_0, \lambda_0} u \sigma dS$$

Reference: Nakamura, N. (1995). Modified Lagrangian-mean diagnostics of the stratospheric polar vortices. Part I. Formulation and analysis of GFDL SKYHI GCM. *Journal of the Atmospheric Sciences*, 52(11), 2096–2108.

# Characterizing quasi-biweekly variability of the Asian monsoon anticyclone using potential vorticity and large-scale geopotential height field

Arata Amemiya<sup>1</sup> and Kaoru Sato<sup>2</sup>

<sup>1</sup>RIKEN Center for Computational Science, Kobe, Japan

<sup>2</sup>Department of Earth and Planetary Science, Faculty of Science, The University of Tokyo, Tokyo, Japan

**Correspondence:** Arata Amemiya (arata.amemiya@riken.jp)

**Abstract.** The spatial pattern of subseasonal variability of the Asian monsoon anticyclone is analyzed using long-term reanalysis data, focusing on the large-scale longitudinal movement. The air inside the anticyclone is quantified by a thickness-weighted low PV area on an isentropic surface. It is shown that the longitudinal movement of the air inside the Asian monsoon anticyclone has a timescale of one to two weeks, which is shorter than the monthly dominant timescale of the variability in the anticyclone intensity. The movement of the anticyclonic air is suggested to be largely controlled by passive advection. The typical time evolution of the variability pattern, explained by two leading EOF components of 100 hPa geopotential height, shows large-scale geopotential anomalies moving westward spanning from low to middle latitudes. This corresponds well with the rapid westward movement of low-PV air known as ‘eddy shedding’ and following eastward retreat of the anticyclonic air. The two EOF components can also explain the bimodal longitudinal distribution of geopotential maximum location.

## 10 1 Introduction

The Asian monsoon anticyclone (hereafter AMA; also known as the South Asian high or the Tibetan high) is characterized by a planetary-scale anticyclonic circulation, which persists in the upper troposphere and lower stratosphere (UTLS) region over the Eurasian continent throughout the northern summer. It is primarily driven by the upper level divergence associated with an extensive latent heat release over the southeast and south Asia induced by the monsoonal deep convection. Recently, this topic attracts increasing attention regarding its important role in the tracer transport between the troposphere and the stratosphere. The Asian summer monsoon region is considered one of the most important pathways of tropospheric tracers entering into the stratosphere. Persistent deep convection transports the air from the boundary layer to the upper troposphere, where the air is mostly confined within the AMA (Dunkerton, 1995; Dethof et al., 1999; Gettelman et al., 2004). The anomalies of various kinds of tropospheric tracers have been observed by satellite-based instruments (Randel and Park, 2006; Park et al., 2007, 2008; Randel et al., 2010; Luo et al., 2018; Santee et al., 2017) as well as in situ measurements by water vapor and ozone sondes (Bian et al., 2012) and aircraft (Gottschaldt et al., 2018). The processes responsible for the tracer transport from the AMA to the lower stratosphere have been intensively studied in recent years using chemical transport models (Park et al., 2009; Vogel et al., 2014, 2016; Pan et al., 2016; Vogel et al., 2019) and trajectory models (Chen et al., 2012;

Garny and Randel, 2016). The large-scale slow upwelling over the AMA is suggested to be ~~dominant~~the dominant transport  
25 process (Garny and Randel, 2016; Vogel et al., 2019). Shorter time-scale processes associated with the subseasonal variability of the AMA, such as fast horizontal transport and turbulent mixing on an isentropic surface, also play important roles (Vogel et al., 2016; Pan et al., 2016; Gottschaldt et al., 2018; Fadnavis et al., 2018).

An isentropic potential vorticity (PV) map is a useful illustration of daily evolution of the air around the tropopause, as PV can be approximately considered a passive tracer, which is conserved in inviscid and adiabatic motion (Hoskins et al.,  
30 1985). The AMA can be identified as an area of significantly low PV surrounded by higher PV area, which correspond to tropospheric and stratospheric air, respectively. The large PV gradient near the boundary of the anticyclone is considered a mixing barrier, which keeps the tropospheric chemical characteristic of the air inside the AMA (Ploeger et al., 2015). The method of quantifying the AMA intensity as an area of PV values below a specific threshold has been used to analyze its seasonal and subseasonal variability (Randel and Park, 2006; Garny and Randel, 2013).

35 Aside from the quantity of total area, the horizontal structure of the AMA seen in low PV area also shows a significant variability, with frequent movement, deformation, and occasional splitting. The deformation and splitting of the AMA usually occur towards the west of the AMA center and called ‘eddy shedding’ (Popovic and Plumb, 2001). The possibility of spontaneous generation of such variability can be reproduced by a simple two dimensional dynamical model imposing a localized steady mass source (Hsu and Plumb, 2000). Further, Amemiya and Sato (2018) showed the characteristic longitudinally-  
40 trapped spatial structure of the variability can also be explained by a two dimensional dynamical model, with a little modification in background latitudinal thermal structure. The deformation and splitting of the anticyclone causes the horizontal stirring and irreversible mixing between the air trapped inside the anticyclone and outside stratospheric air (Pan et al., 2016; Gottschaldt et al., 2018). In addition, the shedding of low PV strip can occur eastward toward West Pacific. It also contributes to the tracer transport from the AMA to the midlatitude lower stratosphere (Vogel et al., 2016; Fadnavis et al., 2018).

45 Another important spatial characteristic of the variability of the AMA is the longitudinal movement of the anticyclone center. The occurrence of the longitude of geopotential maximum on 100 hPa shows a well-known bimodal distribution in a wide range of time scales (Zhang et al., 2002). The two modes are called Tibetan and Iranian modes based on the location of the maximum and usually used to classify temporal states of the anticyclone (~~Zhang et al., 2002~~). ~~A~~, although a recent study showed ~~that the bimodality is a robust feature in a wide range of time scales from daily to monthly, although the detailed~~ the robustness of the  
50 representation depends on the choice of reanalysis data set (Nützel et al., 2016).

Compared to the variability in the AMA intensity, which is considered to be predominantly driven by convective activity variability (Garny and Randel, 2013; Nützel et al., 2016), the mechanism of the variability involving the movement and deformation of the anticyclone has not been fully explained so far, although a few possible mechanisms have been suggested.

One mechanism is that the variability can be generated spontaneously by dynamical instability of two-dimensional flow. The  
55 strong horizontal shear of zonal wind on the northern and southern flank made the anticyclone dynamically unstable, which was originally suggested by Krishnamurti et al. (1973). The idea has been also supported by studies using nonlinear models, such as a beta-plane shallow water model with a localized steady forcing (Hsu and Plumb, 2000), and a mechanistic model in

which a strong anticyclone is forced by a prescribed zonal jet over an idealized mountain (Liu et al., 2007). These studies have shown the possibility of the occurrence of westward eddy shedding without temporally varying external forcing.

60 Another possible mechanism is that the variability in the AMA structure including eddy shedding is forced by other localized pattern of subseasonal variability. It is suggested that the event-like westward movement of the anticyclone anomaly often preceded by the burst of deep convection in the southeast Asia (Annamalai and Slingo, 2001; Ding and Wang, 2007; Garny and Randel, 2013; Nützel et al., 2016). Ortega et al. (2017) has shown that the potential vorticity variability over the southern part of the AMA is often related to the convection variability migrating westward from the western Pacific in a quasi-  
65 biweekly timescale. Also, there is a well known teleconnection pattern through the eastward propagation of a quasi-stationary Rossby wave train along the subtropical jet (Terao, 1998; Ding and Wang, 2005, 2007; Kosaka et al., 2009; Branstator and Teng, 2017). The variability in PV structure of the AMA could be influenced by that pattern triggered in the upstream regions. However, the relative importance of these relations and intrinsic dynamics remains largely unclear.

One of the necessary step towards the understanding of the structural variability of the AMA is to objectively describe the  
70 dominant spatial pattern and its time evolution. Although many efforts have been made to extract the dominant variability patterns in Asian summer monsoon region, most analyses have focused on convection or the subtropical jet, not on the anticyclone in the UTLS as a main actor. The spatial characteristic of the variability in PV has been comprehensively described as westward eddy shedding. The concept of eddy shedding is a useful description of the significant event of the AMA variability, but it corresponds to only a part of time evolution, which actually takes place throughout the summer. It has been not clear yet  
75 if the structural variability of the AMA follows any particular pattern of time evolution or not.

Thus, the purpose of this study is to give a unified view of the dominant pattern of the variability of the AMA, incorporating the existing descriptions, namely, the event-like westward shedding of anticyclonic vortex with low PV air, and the longitudinal movement of the maximum geopotential height location, each of which has been separately discussed in different contexts so far. Based on that, this study attempts to give an implication for the responsible mechanism, which drives the variability.

80 The remainder of this paper is organized as follows: In section 2, the data and analysis methods used in this study are described. In section 3, the sub-seasonal variability of the AMA is analyzed by the method using low PV area, focusing on the longitudinal structure changes. In section 4, the time evolution of the dominant variability pattern of the AMA is examined using an empirical orthogonal function (EOF) decomposition of geopotential field and the relation to the pattern seen in the distribution of low PV area is discussed. Section 5 provides the summary of this paper and discussions regarding the mechanism  
85 of the variability and the relationship with other patterns in similar time scale found in previous studies.

## 2 Data and methods

### 2.1 Reanalysis and observational data

Dynamical variables from the ERA-Interim reanalysis data (Dee et al., 2011) at pressure levels with  $1.5^\circ \times 1.5^\circ$  horizontal resolution are used for the analysis. Variables in the isentropic coordinates are obtained at every 5 K by a vertical interpolation  
90 of the original data. Analyzed time period is June-August of 1979 to 2016. Daily outgoing longwave radiation (OLR) data from

the National Oceanic and Atmospheric Administration (NOAA) (Liebmann and Smith, 1996) for years from 1979 to 2016 are used as a proxy of convective activity.

## 2.2 PV-based metrics of the anticyclone

The intensity and longitudinal distribution of the AMA is quantified using a method based on isentropic PV in this study.

95 The method of identifying a vortex as an area enclosed by contours of a specific reference PV value has been originally developed for studies on the stratospheric polar vortex. It has been mainly used for two purposes. First, it provides the metric of the vortex intensity, which is directly related to irreversible time evolution, assuming that PV is approximately conserved (Butchart and Remsberg, 1986). Second, the edge of the polar vortex as a meridional transport boundary can be objectively detected as the maximum position of PV gradient (Nakamura, 1996; Nash et al., 1996). The calculation of the gradient is  
100 performed with respect to equivalent latitude (Norton, 1994). The advantage of these PV-based methods is that it can quantify the vortex intensity change due to diabatic and turbulent processes, regardless of the reversible perturbation caused by Rossby waves.

Similar methods have been applied to the analysis of the AMA, as it is a planetary-scale coherent vortex as large as the polar vortex. The total area enclosed by a specific PV contour is used to analyze the variability in the AMA intensity  
105 (Randel and Park, 2006; Garny and Randel, 2013). Also, Ploeger et al. (2015) attempted to objectively determine the location of transport barrier using PV and successfully showed that the barrier can be described using temporal PV value in mid-summer. The estimated location of barrier accords well with the position of discontinuity in mixing ratio of atmospheric minor species observed by satellite instruments.

However, the applicability of the methods developed for the polar vortex to the AMA is not straightforward. The AMA is not  
110 a circumpolar but a zonally-elongated elliptic vortex centered at low latitudes. Thus the theories underlying two-dimensional mixing barrier such as the effective diffusivity (Nakamura, 1996) are basically inapplicable. Moreover, ~~as cautioned by Pan et al. (2012), the isentropic surfaces in the UTLS often have steep slopes and therefore show significantly different thickness between the troposphere and the stratosphere (Pan et al., 2012). This may cause the change in~~ the area enclosed by a PV contour ~~is not strictly conserved in the UTLS because of various, even without~~ external forcing processes such as deep convection ~~and the significant thickness variation attributable to the coexistence of tropospheric and stratospheric air.~~

The use of the total area inside a reference PV contour is an effective way to quantify the intensity of the anticyclone, as it measures the intensity of the vortex regardless of its location and structure. On the other hand, the variability in the location and structure of the AMA, which also occurs in a daily timescale and not measured by the total area, is also important. Thus, in this study, not only the total area of the low-PV air but also its longitudinal distribution is examined.

120 The total area as a function of time is described as  $A_{\text{tot}}(t)$  in the following. The time evolution of  $A_{\text{tot}}(t)$  is derived from the PV tendency equation (Butchart and Remsberg, 1986; Garny and Randel, 2013) as follows,

$$\frac{d}{dt} A_{\text{tot}}(t)_{q \leq q_0} = \oint_{q=q_0} \left( -q \frac{\partial \dot{\theta}}{\partial \theta} + \dot{\theta} \frac{\partial q}{\partial \theta} \right) \frac{dS}{|\nabla_{\theta} q|} + \int_{q \leq q_0} \nabla \cdot \hat{\mathbf{u}} dA + (\text{subgrid scale mixing term}) \quad (1)$$

where  $\dot{\theta}$  is the potential temperature tendency by adiabatic processes,  $\mathbf{u}$  is horizontal wind vector,  $dA$  and  $dS$  are respectively an area element and a line element of contours surrounding  $A(t)$ . Variable  $\mathbf{u}$  is decomposed into resolved ( $\hat{\cdot}$ ) and unresolved ( $\cdot'$ ) components as  $\mathbf{u} = \hat{\mathbf{u}} + \mathbf{u}'$ . The terms on the right hand side are called the generation term, divergence term, and mixing term, respectively (Garny and Randel, 2013). Although the direct quantification of each term from gridded reanalysis data is difficult, it was shown by Garny and Randel (2013) using a free-running general circulation model that the first and second terms are well correlated and hence the second term alone can be used as a proxy of convective activity.

To quantify the longitudinal movement of the low PV air, a function of longitude and time  $L(\lambda, t)$ , which has a unit of length, is defined so that its longitudinal integration gives a low-PV area.

$$A(t)_{q \leq q_0} = \int_{\lambda_w}^{\lambda_e} L(\lambda, t) d\lambda, \quad (2)$$

where  $\lambda_w$  and  $\lambda_e$  are arbitrary longitudes. The partial area of low PV air of the AMA on the west of a specific longitude  $\lambda_0$  is obtained by the integration from the western boundary of the calculation domain to  $\lambda_0$  denoted as  $A_{\text{west}}(t)$ . The integration over the entire domain produces  $A_{\text{tot}}(t)$ .

Another treatment that is newly introduced in this study is the weighting of low-PV area by equivalent thickness in isentropic coordinates  $\sigma = -g^{-1} \partial p / \partial \theta$ . Large variation of  $\sigma$  in time and latitude significantly modifies the budget calculation both in seasonal mean and in subseasonal variability, as was indicated by Pan et al. (2012). In this study, instead of using  $L$  and  $A$ , thickness-weighted quantities denoted by  $\hat{L}$  and  $\hat{A}$  are used. The weighted low-PV area  $\hat{A}$  is defined as follows,

$$\hat{A}(t)_{q \leq q_0} \equiv \int_{q \leq q_0} \sigma dA = \int \int \sigma r^2 \cos \phi d\lambda d\phi, \quad (3)$$

where  $r$  is the radius of the Earth.  $\hat{A}$  has an unit of mass divided by a temperature unit. Thus this quantity can be interpreted as a total mass of the air inside the AMA on an isentropic layer with an unit thickness in potential temperature.  $\hat{L}$  is related to  $\hat{A}$  in a similar way as follows,

$$\hat{A}(t)_{q \leq q_0} \equiv \int_{\lambda_w}^{\lambda_e} \hat{L}(\lambda, t) d\lambda \quad (4)$$

The equation for the tendency of mass-weighted total area  $\hat{A}_{\text{tot}}(t)$  takes the following simpler form. See Appendix B for the derivation.

$$\frac{d}{dt} \hat{A}_{\text{tot}}(t) = \oint_{q=q_0} \left( -q \frac{\partial \dot{\theta}}{\partial \theta} + \dot{\theta} \frac{\partial q}{\partial \theta} \right) \frac{\sigma dS}{|\nabla_{\theta} q|} - \int_{q \leq q_0} \frac{\partial}{\partial \theta} (\sigma dS \dot{\theta}) dA + (\text{subgrid scale mixing term unresolved term}) \quad (5)$$

Further, the budget of the mass-weighted partial area to the west of specific longitude  $\lambda_0$  changes due to mass-weighted zonal flux of low-PV air  $\hat{F}(\lambda_0)$ , in addition to the nonconservative terms :

$$\frac{d}{dt} \hat{A}_{\text{west}}(t) = -\hat{F}(\lambda_0) + \oint_{q=q_0, \lambda \leq \lambda_0} \left( -q \frac{\partial \theta}{\partial \theta} + \theta \frac{\partial q}{\partial \theta} \right) \sigma dS - \int_{q \leq q_0, \lambda \leq \lambda_0} \frac{\partial}{\partial \theta} (\sigma \theta) + (\text{subgrid scale mixing term}) (\text{unresolved term}) \quad (7)$$

$$150 \quad \hat{F}(\lambda) = \int_{q \leq q_0} u \sigma r d\phi$$

The flux  $\hat{F}(\lambda_0)$  represents the movement mass flux of low PV air in the zonal direction through-at the longitude  $\lambda_0$ , integrated over the latitude where the PV is below the threshold. Comparing the left hand side and the flux term on the right hand side, the relative contribution of the movement of anticyclonic air due to conservative processes can be quantified.

155 The Eq. 3 and Eq. 5 have no divergence term, which is present on the right hand side of Eq. 1. This implies that, by the thickness weighting,  $\hat{A}$  changes only when there is non-conservative forcing such as diabatic heating. Therefore, the  $\hat{A}$  can be interpreted as an equivalent 2-d representation of the air parcel. In other words, this formulation separates the effect of horizontal divergence induced by the diabatic heating from that induced by compression or tilting of the air parcel by the steep slopes of isentropic surfaces. The tendency of  $\hat{A}_{\text{west}}$  is mostly explained by the longitudinal flux term  $\hat{F}(\lambda)$  when other nonconservative processes over the area of  $\hat{A}$  are negligible. Note that this formulation is different from that based on  
 160 the thickness-weighted PV flux introduced by Ortega et al. (2018), in that our formulation identifies the AMA by using the PV-based coordinate. The flux term  $\hat{F}(\lambda)$  represents the mass flux of low PV air, not the PV flux. This means, given that the threshold PV value properly reflects the mixing barrier, the flux of low PV air implies how atmospheric chemical tracers are distributed, even when a local value of PV changes in the regions where PV is below the threshold. As an illustrative example, Fig. 1a shows a PV field on the 370 K isentropic level on a specific day. The area of PV values below 2 PVU is hatched by red dots. Figure 1b shows the distribution of horizontal winds and thickness  $\sigma$  inside the AMA. Strong anticyclonic circulation is seen along the boundary of the area. Larger values of thickness are found in the northern part of the area compared to the southern part, indicating the necessity-effectiveness of thickness-weighting.

170 The analysis is generally sensitive to the choice of reference isentropic level, PV threshold, and calculation domain. In this study, the horizontal area 10°W–160°E, 10°N–50°N is examined. The reference PV value, isentropic surface, and the analysis domain in this study are compared to the previous studies, which used the similar method (Randel and Park, 2006; Garny and Randel, 2013; Ploeger et al., 2015) in Table 1. Budget calculations are performed for three respective isentropic levels of 360 K, 370 K and 380 K using the PV thresholds shown in Table 1. A detailed analysis is mainly performed for July and August on the 370 K level, where the PV gradient is the largest. The detailed reasoning for these reference values is described in the Appendix Appendix A.

**3.1 Total thickness-weighted area**

Figure 2 shows the time series of thickness-weighted low PV area defined on 360 K and 370 K isentropic levels, along with the time series of area-averaged OLR over 15°N – 30°N, 60°–120°E from June to August. The result for a specific year 2016 is shown as an example. Thick lines represent lowpass-filtered 1979–2016 mean with a cut-off length of 31 days. The mean seasonal evolution of weighted low PV area during summer has a peak in the middle of July. The total low PV areas measured at 360 K and 370 K in 2016 both fluctuate with a time scale near 30 days including minima in late June and late July, and maxima in mid July and mid August. There is also a steep maximum in the middle of June both in low PV area and OLR, implying an event with a shorter timescale. There is a clear correspondence between fluctuations in total low PV area and area-averaged OLR in this year with about a few days lag, especially for 360 K, as pointed out by previous studies (Randel and Park, 2006; Garny and Randel, 2013).

**3.2 Longitudinal movement of the air inside the AMA**

~~The analysis regarding Previous studies used the total area  $\hat{A}_{\text{tot}}$  so far confirmed that the period comparable to or longer than quasi-biweekly timescale is dominant for the variability of the AMA intensity has been used, without weighting, to analyze the AMA variability and found the dominant timescale around 30 days.~~ However, the use of total area ~~cannot describe does not take account of~~ the zonal displacement and deformation of the AMA which may have different timescales and patterns, such as those described as the 'eddy shedding'. The longitudinal distribution of low PV area is analyzed in ~~the following our study as in the following.~~

Figure 3 a shows an average of the zonal flux of thickness-weighted area of low PV air (Eq. 7) as well as the standard deviation as a function of the longitude on ~~the each of the 380 K, 370 K, and 360 K~~ level for July and August of 1979-2016. ~~The At 370 and 380 K, the~~ mean zonal flux is slightly eastward ~~but almost zero~~. The standard deviation is much larger and maximized in the longitudinal region of about 40°E – 100 °E. This implies that the area of low PV air oscillates zonally within this longitudes while time-mean zonal movement of air is relatively insignificant on this level. Note that the mean flux of low PV air does not need to be zero because it can be balanced with nonzero PV source/sink by differential radiative heating which is significant in seasonal mean and largely depends on the vertical levels. ~~Fig. 3b show the result for 360 K. The mean zonal flux is largely negative between 30E and 120E. The positive zonal flux divergence in the eastern part is likely generated by convective forcing, while the positive flux convergence in the western part can be balanced by the sink in low PV area due to large vertical gradient in radiative heating/cooling around the 360 K level.~~

The important feature observed both in Figs. 3a and b is large fluctuations in the zonal flux of low PV air as shown by the large standard deviations. This implies that a large part of the air mass inside the AMA can move eastward and westward. This is consistent with the results of trajectory analysis by Garny and Randel (2016), in which passive tracers released within the anticyclone tend to be trapped inside for about a month on average. ~~At 360 K, the mean zonal flux is largely negative between 30°E and 120°E. The positive zonal flux divergence in the eastern part is likely generated by convective forcing, while the~~

positive flux convergence in the western part would be balanced by the sink in low PV area due to large vertical gradient in radiative heating/cooling around the 360 K level.

210 Figure 4 shows the longitude-time cross section of thickness-weighted anticyclone area fraction  $\hat{L}(\lambda, t)$  calculated for each longitudinal grid interval and its zonal flux  $\hat{F}(\lambda, t)$  at 360, 370, and 380 K. Results for the summer months of 2016 is are shown for example. Frequent zonal movement of the anticyclone air with a sub-monthly timescale can be is clearly seen. Similar feature has already been illustrated by simple longitude-time plots of geopotential height or PV in several previous studies (Garny and Randel, 2013; Ortega et al., 2017). However, they are found in previous studies, but most of them showed only variables averaged over a fixed range of latitude in the southern part of the AMA. Thus, the whole picture of the variability cycle may not be captured. Specifically, they may miss the longitudinal structure change after eddy shedding events has been not clearly described. An advantage of using  $\hat{L}$  in Fig. 4 is that it enables us to examine the quantitative details of. The view based on the low-PV area, first introduced by Garny and Randel (2013), is useful to capture the zonal movements of the AMA regardless of latitudinal position, as far as the approximation of PV conservation holds. Large pulses of its latitudinal position.

220 Figure 4 is similar to thier Fig. 6, except that the weighted values are used and the zonal flux  $\hat{F}$  is added. At 360 K, the longitudinal flux is mainly westward. At 370 K and 380 K, in contrast, the pulses of both westward and eastward fluxes flux occur alternately in July in the region of 30 °E–120 °E. The budget of the low PV air shows different characteristics at each of these levels. The alternate eastward and westward movements at 370 K imply that the variability is more like oscillatory behavior rather than dissipative westward eddy shedding as reproduced by a two dimensional model (Hsu and Plumb, 2000).

225 The daily evolution of the time tendency of partial thickness-weighted area  $\frac{d}{dt} \hat{A}_{west}$  at 360 K, 370 K and 380 K on the west of 60 °E and the contribution from the zonal flux  $\hat{F}_{\lambda=60^\circ}$  through that longitude are shown in Fig. 5. The two lines At 370 K, the two curves correspond with each other very well regardless of the sign, except in the beginning of June when the noise in PV-based definition around the southern boundary could be large. The correlation coefficient between these two terms calculated from the time series for 1979-2016 is as high as 0.663. This result means that the oscillation of the AMA at this level is mostly due to a simple zonal advection, and other effects such as dissipation by turbulent mixing are secondary. Therefore, the zonal flux flux At 360 K, the two curves still show the variability synchronized with each other, but with a large offset. This implies the existence of a large sink of low PV area at 360 K. At 380 K, the two curves also accord well with each other, although large disagreements are occasionally observed. This may imply sporadic nonconservative processes at this level. Note that the disagreement may be just due to the error in calculating  $\hat{A}_{west}$ , which is more likely to occur at 380 K than at lower levels (See

235 Appendix A). While the whole picture to explain the budget of low PV area at these levels is more complicated than what is seen at a single level, we consider the longitudinal oscillatory behavior with a submonthly time scale is one of the important features of the variability of AMA, and the zonal flux  $\hat{F}_{\lambda=60^\circ}$  can be considered a representative variable describing the zonal oseeillation of the AMA in subseasonal timescale at 370 K as a representative variable for it. This variable will be used as a proxy of the zonal movement of the AMA in the composite analysis in next section.

240 Figure 6 shows the power spectrum at 370K of the zonal flux  $\hat{F}_{\lambda=60^\circ}$  as a 38-year mean. There is a significant peak around broad peak between about 9 day, which is shorter than and 20 days, and no peak is found around 30 days, which corresponds to the dominant period of the variability in total low PV area. Thus the dominant time scale of the subseasonal variability with

~~the longitudinal movement and deformation of the AMA should be shorter than that of the variability~~ of the AMA intensity shown in Garny and Randel (2013). This supports the idea that the variability pattern with the zonal movement of the AMA ~~can be is~~ effectively separated by extracting short-period components of the variability, including the quasi-biweekly timescale mentioned in previous studies. For this reason, the ~~time scale around the quasi-biweekly period~~ quasi-biweekly time scale is focused on in the following analyses.

## 4 The life cycle of quasi-biweekly oscillation of the anticyclone

### 4.1 EOF decomposition

250 The life cycle of the dominant large scale pattern of the subseasonal variability of the AMA is examined using the empirical orthogonal function (EOF) decomposition. The EOF analysis is applied to the daily-mean geopotential anomaly ~~with time periods of 5–20 days~~ in the domain covering the AMA using ERA-Interim reanalysis data. Before calculating EOFs, anomalies are filtered with a band-pass filter within time periods of 5–20 days, normalized at each grid point ~~by dividing~~, divided by their standard deviations and weighted by the square root of grid areas. In other words, decomposition is performed for correlation 255 matrix weighted by each grid area instead of covariance matrix. The normalization is effective to reduce the effect of the latitudinal dependence of geopotential height perturbation amplitude. Otherwise the perturbation patterns would be concentrated at midlatitudes and coherent low latitude features may be missed. The analysis is made for the regions of 0°E–150°E, 10°N–50°N at 100 hPa and July and August of 1979–2016. EOFs for longer ~~months period~~ such as June to September, for slightly different levels such as 150 and 200 hPa, or for a slightly different horizontal domain do not differ much. It was confirmed 260 that extended EOF and complex EOF analysis provides essentially similar spatial patterns (not shown). Thus, only the results obtained by a standard EOF analysis are shown.

The first two EOF components are dominant and sufficiently separated from others by North's rule of thumb (North et al., 1982). The partial variance explained by those two components are about 15% and 13%, respectively. The spatial structures of geopotential height of the two components are shown in Fig. 7. Both EOF1 and EOF2 have large-scale longitudinal wavy 265 patterns approximately from 0°E to 120°E over low and mid latitudes. The combination of these two components explain about 30 % of zonally averaged total perturbation variance. Note that this latitudinal structure having large amplitudes both in low and mid latitudes is different from well-known patterns extracted by EOFs for meridional wind perturbations (Kosaka et al., 2009) or ~~simple correlations with a time series at a point at a midlatitude~~ the composite analysis for the extreme events of positive geopotential height anomaly averaged over 35–45 °N, 55–75 °E (Ding and Wang, 2007). The pattern extracted in this 270 study shown in Fig. 7 has larger scales than those previous studies. This is likely due to the choice of geopotential height anomaly for the EOF analysis which tends to favor larger-scale structure than other variables such as meridional wind.

The time series of principle components (PCs) 1 and 2, corresponding to two leading EOFs, have significant lag correlation with each other, as shown in Fig. 8. PC1 is lagged behind PC2 by about 3 days. As EOF2 has the structure which is out of phase by about a quarter cycle with EOF1, indicating the dominance of westward propagation of wavy patterns.

275 Eight phases are defined based on normalized PC1 and 2 time series, as illustrated in Fig. 9. The daily states are labeled as each of these phases when geopotential perturbation amplitude projected onto that two dimensional phase space exceeds unity. The summary of phase progress statistics is shown in Fig. 10. For more than 50% cases, the phase progresses to the next within one day. And for more than 60% cases it does within two days. It is also shown that the reverse progress rarely occurs. This implies the transition from a phase to the next one mostly takes place within two days, which is consistent with lead time in  
280 Fig. 8 and corresponds to the quasi-biweekly dominant timescale found in section 3. Based on these facts, the characteristics of the time evolution of the AMA variability pattern are examined by composite mean maps for each phase.

#### 4.2 Composite life cycle of the AMA variability pattern

First, the life cycle of the extracted disturbance is examined in terms of the intensity, location and structure of the AMA based on the low PV area with a PV threshold of 2 PVU on the 370 K isentropic level (see section 2.4). Figure 11 shows maps of  
285 the frequency of existence of the low PV air for each phase. The area with a percentage greater than 60 % are color-shaded. ~~The area of high frequency of low PV air moves westward as~~ As the phase progresses from phase 4 to phase 1. ~~The feature of eddy shedding is seen during the progress from phase~~ 6 through phase 1, ~~in which~~ a large portion of high frequency area moves westward and reaches around 30°E. After that, the high frequency area drifts slightly northward and moves eastward back from phase 2 to phase 4. This zonal oscillatory behavior is almost consistent with the large fluctuation of zonal flux of low PV air  
290 observed in longitudes from 30°E to 110°E in Fig. 3. The zonal movement with the phase progress is quantitatively shown as a composite mean of the thickness-weighted zonal flux of low PV air at 370 K at 60°E (Fig. 12). The flux has negative (i.e. westward) peak around phase 6 and positive (eastward) peak around phase 3. Fig. 13 shows the mean area of the whole AMA and partial area at 370 K to the west of 60°E for each phase. Standard deviation is also shown by dashed curves. The western part ~~fluctuate~~ fluctuates with phase, as it is largely controlled by the zonal flux in weekly timescale (Fig. 5). In contrast, the  
295 total area does not show significant dependence on the phase. ~~This implies the pattern of the variability is not affected largely by the~~ As the total area is likely to be controlled by the total intensity of the thermal forcing, ~~because this implies that the variability in~~ the thermal forcing ~~should directly lead to the change of the total area of the AMA~~ intensity is not a key factor for this variability pattern. This supports the idea that the variability in the weekly biweekly timescale is determined by internal dynamics.

300 Next, the spatial characteristics of geopotential and the variables related to convective activities during the phase progress are examined. Composites of geopotential (black contours) and its anomaly from climatology (color shades) on 100 hPa along with OLR anomalies [red(positive) and green(negative) contours] are shown in Fig. 14. As already seen in Fig. 7, geopotential anomaly exhibits large-scale wave-like pattern propagating westward along the subtropical jet about 40°N – 50°N. The geopotential anomalies are extended southeastward to low latitudes. The positive geopotential anomaly along 30°N  
305 is located at about 70°E at phase 5, 50°E at phase 6, 40°E at phase 7, and 30°E at phase 8. The westward movement of positive geopotential anomaly follows roughly the movement of high occurrence of low PV area from phase 5 to phase 8 (Fig. 11).

Statistically significant OLR anomalies are found mainly over Tibetan Plateau, southern China, and the region from northern Bay of Bengal to northern India. The anomalies over the Tibetan Plateau is in phase with geopotential anomalies of the same

sign. Over other two regions, the relation of the OLR anomalies with geopotential anomalies and with PV distribution (Fig. 11) is less clear. The observed convection variability may occur in response to the large scale dynamical variability, and/or have an influence on the dynamics. This point will be discussed in the next section.

Fig. 15a and 15b show the geopotential anomalies averaged over 15°N–25°N and 35°N–45°N, respectively, in the longitude-pressure cross sections. Color shading shows the geopotential anomalies from the climatology, whereas contours show the anomalies from longitudinal mean to indicate the AMA center location. Only results for phases 1 to 4 are shown, as the features for ~~rest the rest of the~~ phases appear close to the negative counterparts. The longitude-pressure structure of the anomalies is almost barotropic in both the low and middle latitudes. The amplitude of the anomalies is maximized around 100 hPa for the low latitudes and around 150–200 hPa for the midlatitudes, reflecting the difference in the tropopause height. The level of the maximum roughly corresponds to the tropopause level. Thus it is considered that the pattern is essentially trapped by the tropopause, as is the AMA itself (Popovic and Plumb, 2001). For the low latitudes, significant anomalies are observed down to about 400 hPa, close to the level where the convective thermal forcing is maximized. In contrast, vertical structure is the deeper at ~~midlatitudes. This is probably related to the existence of the subtropical jet associated with thermal gradient around~~ midlatitudes.

### 4.3 The relation with the bimodality in anticyclone center location

The bimodality of the center longitude seen at 100 hPa is one of the important characteristics of spatial variability of the AMA. The relation between the bimodality and the quasi-biweekly AMA variability pattern defined in this study is examined.

Using the ERA-Interim reanalysis data from July to August of 1979-2016, the longitudinal distribution of the AMA center, that is defined as the location of daily mean geopotential height maximum, is calculated. The total distribution is shown in the bars in Fig. 16. The bimodal distribution with peaks around 60 °E and 90 °E is observed. The distribution is also calculated separately for each phase, as shown in curves in different colors in Fig. 16. Numerals show the location of peak longitudes for respective phases. There is a clear phase dependence of the distribution. Phases 1 to 3 favor the eastern location around 90°E of the AMA center, while phases 5 to 8 favor the western location around 60°E. This phase dependence can be mostly explained by the spatial structure of EOF2 shown in Fig. 7(b). The partial variance explained by EOF2 component is sufficiently large to enable large positive and negative EOF2 components to contribute to eastward and westward displacement of the AMA center, respectively.

## 335 5 Summary and Discussion

In this study, the subseasonal variability of the AMA, which includes longitudinal movements on a quasi-biweekly time scale was examined. The analyses were performed from two different perspectives, that is, the movement of the air inside the AMA defined as thickness-weighted low PV area and an EOF decomposition of normalized geopotential anomaly field on 100 hPa.

The zonal distribution of thickness-weighted low PV area and its zonal flux was calculated using ERA-Interim reanalysis data from 1979 to 2016. The longitudinal distribution of low PV area in mid-summer exhibits a significant temporal fluctuation.

The budget analysis revealed that the tendency of the partial thickness-weighted low PV area on the west of the specified longitude of 60 °E is mostly controlled by the zonal flux entering the domain on a subseasonal time scale. This suggests that the variability is mostly controlled by the large scale dynamics, and other nonconservative processes such as turbulent dissipation and diabatic heating by radiation and/or convection have secondary roles on this time scale. Thus the variability can be characterized as event-like pulses of zonal flux of low PV air at the longitude around 60 °E, ~~consistent with the notion of 'eddy-shedding'.~~

The ~~dominant~~ large-scale variability pattern in geopotential height on a pressure level around the tropopause was ~~mostly~~ reconstructed by the first two EOF components. They explained about 30% of the total variance and are significantly separated from other components. They had large scale anomaly patterns spanning from middle to low latitudes with comparable amplitudes and a significant lead-lag correlation with each other. The reconstructed pattern by these two components showed a westward-moving large scale geopotential anomaly. By defining the phase of this pattern based on a two-dimensional phase space by these leading modes, spatial structures of variables at each phase in the whole life cycle were examined. The distribution of the occurrence frequency of low PV on 370 K level indicated clear zonal oscillation of the air inside the AMA as phase progresses. There was a significant relationship between the phase and zonal flux of low PV air, as the rapid westward movement around 60 °E at phase 6 in Fig. 11 corresponds to large westward flux of low PV air in Fig. 12. Composite of geopotential height shows the westward-propagating large-scale anomaly pattern along the subtropical jet. The vertical structure is nearly barotropic in both middle and low latitudes. The influences down to the level of middle troposphere was observed at the midlatitude, whereas at the low latitude disturbances are largely trapped above 300 hPa.

The variability pattern revealed in this study has a robust tendency of cyclic time evolution (Fig. 10) in which a quasi-biweekly time scale is dominant. Thus an important question is what drives this variability and determines the time scale. The driver of the AMA variability has been discussed in previous studies focusing mainly on seasonal evolution and longer period variability patterns. For the variability in the anticyclone intensity with a monthly time scale, the essential role of the variability in convection in south to southeast Asia has been suggested (Garny and Randel, 2013; Nützel et al., 2016). However, it is not straightforward the similar relationship applies to the quasi-biweekly variability focused on in this study. ~~Figure 14 shows the statistically significant negative OLR anomalies in southern China and northeastern to northern India in phase 6. However, the intensified convection over the northern Bay of Bengal and the westward expansion of low PV area do not accord. In phase 6 and 7, when the composite mean horizontal divergence anomaly on the 360 K level is the largest over the Bay of Bengal, the main part of the AMA measured as low PV area is most likely to be already located to the west on intensified convection area. This implies the westward movement of low PV area is not necessarily forced or triggered by a temporal burst of monsoonal convection.~~

The causal relationship between convective variability and the UTLS circulation variability ~~focused on in this study in the~~ quasi-biweekly timescale remains an important question. There have been a few studies, which suggest variability patterns coupled with convection anomalies of smaller spatial scale over the area including the Tibetan Plateau, east Asia, south Asia, and the western Pacific. For example, Fujinami and Yasunari (2004) suggested a cyclic pattern of convective anomalies propagating clockwise from Tibetan Plateau via south China and northeast India, along with Rossby wave train over the subtropical jet.

Also, a recent study by Ortega et al. (2017) has examined the coupling between quasi-biweekly variabilities in tropospheric convection and the UTLS dynamics, suggesting the possibility that the latter one leads the former. However, as they used area-averaged PV over southern India for a metric of upper tropospheric disturbances, their results have captured the pattern significant for the southeastern part of the area of AMA, not the whole extent of AMA, which includes midlatitudes and west Asia. In this study, the statistically significant pattern of OLR anomalies was found in the composite analysis based on the EOF leading components of dynamical field perturbations (Fig. 14). This anomaly pattern of convection may be the response to the dynamical variability, or rather the driver of the variability. A recent study by Wei et al. (2019) suggested the latter possibility based on their composite analysis focusing on the longitudinal movement of the AMA center. However the spatial location of the OLR anomalies corresponding to each of the phase of the AMA variability found in this study does not necessarily support it. For example, in phase 6, there are significant negative OLR anomalies over southern China and northeastern to northern India. This feature indicates the intensified convection and the explanation of low PV area by upper tropospheric horizontal divergence over these areas. However, at this phase, the maximum low PV area probability in Fig. 11 is located around 50-80 °E, to the west of the area of intensified convection. This mismatch implies that the westward movement of low PV area is not forced or triggered by a temporal burst of monsoonal convection over the northeastern to northern India, provided that this phase progress based on the EOF analysis properly captures the characteristic time evolution of dynamical fields associated with the variability pattern. The relationship between ~~these existing patterns and the~~ the anomaly pattern found in this study and that of previous studies should be explored in future studies.

The subseasonal variability pattern can be driven by dynamical instability of two dimensional anticyclonic flow, as mentioned in section 1. The essentially barotropic structure of the anomalies seen in Fig. 15 supports the validity of a conceptual two dimensional model to explain the dynamics. The analysis in this study using thickness-weighted low PV area and its zonal flux showed the pulse of westward movement of low PV air characterizing the variability. This behavior corresponds to spontaneous eddy shedding reproduced by the two dimensional model in a previous study (Hsu and Plumb, 2000). However, there is an essential difference between their modeled eddy shedding and the observed variability in terms of the budget of low PV area. Whereas anticyclonic eddies dissipate after westward shedding in the conventional dynamical model, the low PV area in reality does not dissipate but mostly returns eastward and forms the oscillatory pattern seen in Fig. 11 and Fig. 12. A recent study attempts to explain this behavior, using a modified two-dimensional dynamical model, which includes the effect of latitudinally-varying tropopause structure (Amemiya and Sato, 2018).

The zonal oscillation of the AMA viewed as low PV area in this study is directly linked to the oscillation of the mixing ratio anomalies of various atmospheric minor constituents, as PV approximately acts as conserved quantity as well. Irreversible tracer transport through the AMA occurs with several dynamical or physical processes. Those are dependent on the temporal structure or position of the AMA during the subseasonal variability. For example, the large scale upwelling, which transports the air into the tropical lower stratosphere, may correspond to the temporal position of the AMA. Turbulent mixing can be enhanced in the process of eddy shedding. Also, occasional westward or eastward shedding of tropospheric air out of the AMA, which contributes to the transport to the midlatitude stratosphere (Vogel et al., 2016), may be dependent on the phase of large scale variability described in this study.

Additionally, the understanding of the dynamics of the AMA and its relation to tropospheric weather patterns is practically important. The subseasonal variability of the Asian summer monsoon is one of the most essential factors in predicting the risk of high impact weather such as heavy rainfall and droughts in south and southeast Asia. For the practical purpose, describing the dominant variability patterns and their typical time evolution provides a useful framework for a subseasonal prediction, as  
415 has been successfully applied to Madden-Julian Oscillation. Recent studies have found several dynamical predictors for heavy rain events (Ding and Wang, 2009) and introduced real-time multivariate indices for the variability of the Asian summer monsoon (Lee et al., 2013). The pattern discussed in this study based on low PV area and geopotential anomalies focuses on a wider area from middle east to east Asia including the Tibetan Plateau. The relative importance of this variability pattern for local precipitation prediction and the relation to existing patterns is an interesting topic for future study.

420 *Data availability.* The ERA-Interim data was downloaded from the ECMWF data server (<http://apps.ecmwf.int/datasets/>, last access: 26 April 2020). Daily outgoing longwave radiation (OLR) data was downloaded from the NOAA PSL server ([https://psl.noaa.gov/data/gridded/data.interp\\_OLR.html](https://psl.noaa.gov/data/gridded/data.interp_OLR.html), last access: 26 April 2020).

#### **Appendix A: The choice of reference PV, isentropic level and southern boundary latitude of the domain**

In this study, the area of the anticyclone is defined as the area in which PV is lower than a specific reference value. The domain  
425 used for this analysis should be specified by certain ranges of longitude and latitude where the AMA is typically found. The proper choice of such longitude and latitude ranges, as well as the reference PV value and isentropic level, is not a trivial issue, because the boundary of the AMA is not always well-defined by a fixed value of PV, especially on its southern flank. As seen in Fig. 1, PV values near the equator are as low as that inside the AMA, although the equatorial UTLS air generally have different origin and does not mix with the air inside the AMA easily, as they are usually separated by the air in low latitudes  
430 with larger PV values. Ideally, by choosing sufficiently low reference PV value and proper position of the southern boundary of the domain, the AMA can be detected as an isolated area of low PV within the domain. However, due to the large subseasonal variability and seasonal evolution of the AMA both in PV value and structure, it is sometimes difficult to isolate the area of the AMA from the equatorial air. When the southern boundary of the domain is located too close to the equator, the equatorial air, which is supposed to be stratospheric origin may be counted as the area inside the AMA. In contrast, when it is located at  
435 higher than the optimal latitude, part of southern portion of the AMA will be excluded. In such a case the AMA intensity is underestimated and the important response to the low latitude convection might be missed. Additionally if the reference PV value is too large, it is not always possible to separate the AMA and the equatorial air by the closed PV contour. Therefore, although these sources of error can not be completely excluded, it is worthwhile to show how and to what extent they can be minimized by the optimal choices of the domain boundary and reference PV and isentropic surface values.

440 In the following, the largest source of error is considered to be generated from the choice of the southern boundary latitude of the domain and a reference PV value, while other boundary positions are fixed. The northern boundary is fixed at 50°N. The

eastern and western boundary are set to 160°E and 10°W, respectively, following Ploeger et al. (2015). It is confirmed that the sensitivities of calculated AMA areas to these values are not significant.

The optimal southern boundary latitude and the reference PV value are explored as follows. On each of the isentropic surfaces 360, 370, and 380 K, the frequency of occurrence of grid points with PV lower than the reference within the longitudinal range (10°W to 160°E) is calculated as a function of latitude. Calculation is performed for each month from June to September, using the 6 hourly ERA-Interim reanalysis data from 1979 to 2016.

Figure A1 shows the results on each of three isentropic surfaces for each month. Generally, the occurrence of low PV air has a peak in subtropical latitudes separated from the high occurrences near the equator. The relative error of the AMA area calculation is implied by the significance of isolation of such a peak. Sufficiently high occurrence of PV lower than the reference value around the subtropical latitudes and infrequent occurrence on the equatorial periphery of the AMA are desirable. Such a contrast is the most clear in July and August at 370 K, when the value around 2 PVU is used as the reference. In June, the AMA areas are almost similar to those in July, although there are higher occurrences in low latitudes. The latitude of maximum occurrence, which roughly corresponds to the AMA center is located southward compared to that in July, and the separation from the equatorial air is less clear. In September, the contrast in occurrence between low latitudes and mid latitudes becomes obscure for most reference PV values. Such behavior with respect to seasonal transition is consistent with the seasonal evolution of the AMA shown in monthly climatology of PV on 370 K isentropes in Fig. A1. The similar seasonal evolution can be observed at other isentropic levels. At 380 K, less significant maximum occurrences in mid latitudes are found. At 360 K, the whole pattern is shifted to lower latitudes and the minimum in low latitudes is more obscure. Considering these results, the value around 2.0 PVU on 370 K isentropic level is implied to be the best reference value. On 360 K and 380 K, the respective reference values should be around 0.5 PVU and 3.5 PVU to describe the anticyclonic vortex while minimizing the noise by the southern boundary.

Those values are also compared with the barrier PV values on each isentropic level, determined objectively following the method by Ploeger et al. (2015). Their criterion to detect mixing barrier is based on the maximum of PV gradient with respect to equivalent latitude defined base on PV (see their section. 4 for the detailed methodology). Using the long-term reanalysis data from 1979 to 2016, we calculated the barrier PV value for each day on each of 360, 370 and 380 K isentropic levels.

Figure A2 summarizes the result. The median (50 percentile) and 15 and 85 percentiles of barrier PV values, along with the ratio of barrier detection in number (%), are shown for each 10 or 11-day month part of the boreal summer season. We found that 370 K is the most favorable isentropic level to detect barrier objectively, with percentages above 60% throughout July and August, although Ploeger et al. (2015) have shown that 380 K provides the most significant barrier feature. This discrepancy can be explained considering that the detectability can vary in interannual and long period intraseasonal timescale, reflecting large dynamical variability. On 360 K, the percentage of barrier detection has lower values compared to 370 and 380 K but still larger than 40 % in July. In July and August, the range of barrier PV values are almost unchanged with respect to time, while in June lower values are more dominant. Median PV values on each of 360, 370 and 380 K levels are near 0.5, 2.0 and 3.5 PVU, respectively. These values are close to optimal values implied by Fig. A1 to detect anticyclonic air sufficiently wide and also separated from the equatorial air.

Supported by these results, we chose the calculation domain and reference values in the following. The domain is chosen to be inside 12–50°N, 10°W–160°E. The reference PV value used for analyses were chosen to be 2.0 PVU on 370 K. The high ~~percentage~~percentage of barrier detection around this value implies the relevance of the underlying concept of isolated strong nearly-inviscid anticyclone, in which low PV air is surrounded by distinct boundary with steep PV gradient. For the purpose of the comparison of zonal anticyclone area flux on different levels, reference values 0.5 and 3.5 PVU were also used respectively on 360 and 380 K. Most analyses were performed for July and August, when the anticyclone is the most intense and the PV-based definition is the most relevant. Three-months data from June to August is only used for the spectrum analyses.

## **Appendix B: Derivation of the tendency equation for the thickness-weighted low PV area**

485 *Author contributions.* AA conducted the data analysis. AA and KS contributed to the discussion and the writing of the paper.

*Competing interests.* The authors declare that they have no conflict of interest.

*Acknowledgements.* This study is supported by the Japan Science and Technology Agency CREST program (JPMJCR 1663) and the Japan Society for the Promotion of Science (JSPS) Grant-in-Aid Scientific Research (A) 25247075 program. All of the figures were prepared using fortran DCL developed by GFD Dennou Club (<https://www.gfd-dennou.org/index.html.en>).

490 **References**

- Amemiya, A. and Sato, K.: A two-dimensional dynamical model for the subseasonal variability of the Asian monsoon anticyclone, *Journal of the Atmospheric Sciences*, 75, 3597–3612, 2018.
- Annamalai, H. and Slingo, J.: Active/break cycles: diagnosis of the intraseasonal variability of the Asian summer monsoon, *Climate Dynamics*, 18, 85–102, 2001.
- 495 Bian, J., Pan, L. L., Paulik, L., Vømel, H., Chen, H., and Lu, D.: In situ water vapor and ozone measurements in Lhasa and Kunming during the Asian summer monsoon, *Geophysical Research Letters*, 39, 2012.
- Branstator, G. and Teng, H.: Tropospheric Waveguide Teleconnections and Their Seasonality, *Journal of the Atmospheric Sciences*, 74, 1513–1532, 2017.
- Butchart, N. and Remsberg, E. E.: The area of the stratospheric polar vortex as a diagnostic for tracer transport on an isentropic surface, *Journal of the atmospheric sciences*, 43, 1319–1339, 1986.
- 500 Chen, B., Xu, X., Yang, S., and Zhao, T.: Climatological perspectives of air transport from atmospheric boundary layer to tropopause layer over Asian monsoon regions during boreal summer inferred from Lagrangian approach, *Atmospheric Chemistry and Physics*, 12, 5827–5839, 2012.
- Dee, D., Uppala, S., Simmons, A., Berrisford, P., Poli, P., Kobayashi, S., Andrae, U., Balmaseda, M., Balsamo, G., Bauer, P., et al.: The ERA-Interim reanalysis: Configuration and performance of the data assimilation system, *Quarterly Journal of the royal meteorological society*, 137, 553–597, 2011.
- 505 Dethof, A., O’Neill, A., Slingo, J., and Smit, H.: A mechanism for moistening the lower stratosphere involving the Asian summer monsoon, *Quarterly Journal of the Royal Meteorological Society*, 125, 1079–1106, 1999.
- Ding, Q. and Wang, B.: Circumglobal teleconnection in the Northern Hemisphere summer, *Journal of Climate*, 18, 3483–3505, 2005.
- 510 Ding, Q. and Wang, B.: Intraseasonal teleconnection between the summer Eurasian wave train and the Indian monsoon, *Journal of climate*, 20, 3751–3767, 2007.
- Ding, Q. and Wang, B.: Predicting extreme phases of the Indian summer monsoon, *Journal of Climate*, 22, 346–363, 2009.
- Dunkerton, T. J.: Evidence of meridional motion in the summer lower stratosphere adjacent to monsoon regions, *Journal of Geophysical Research: Atmospheres* (1984–2012), 100, 16 675–16 688, 1995.
- 515 Fadnavis, S., Roy, C., Chattopadhyay, R., Sioris, C. E., Rap, A., Müller, R., Kumar, K. R., and Krishnan, R.: Transport of trace gases via eddy shedding from the Asian summer monsoon anticyclone and associated impacts on ozone heating rates, *Atmospheric Chemistry and Physics*, 18, 11 493–11 506, <https://doi.org/10.5194/acp-18-11493-2018>, 2018.
- Fujinami, H. and Yasunari, T.: Submonthly variability of convection and circulation over and around the Tibetan Plateau during the boreal summer, *Journal of the Meteorological Society of Japan. Ser. II*, 82, 1545–1564, 2004.
- 520 Garny, H. and Randel, W.: Dynamic variability of the Asian monsoon anticyclone observed in potential vorticity and correlations with tracer distributions, *Journal of Geophysical Research: Atmospheres*, 118, 13–421, 2013.
- Garny, H. and Randel, W. J.: Transport pathways from the Asian monsoon anticyclone to the stratosphere, *Atmospheric Chemistry and Physics*, 16, 2703–2718, 2016.
- Gettelman, A., Kinnison, D. E., Dunkerton, T. J., and Brasseur, G. P.: Impact of monsoon circulations on the upper troposphere and lower stratosphere, *Journal of Geophysical Research: Atmospheres* (1984–2012), 109, 2004.
- 525

- Gottschaldt, K.-D., Schlager, H., Baumann, R., Cai, D. S., Eyring, V., Graf, P., Grewe, V., Jöckel, P., Jurkat-Witschas, T., Voigt, C., et al.: Dynamics and composition of the Asian summer monsoon anticyclone, *Atmospheric Chemistry and Physics*, 18, 5655, 2018.
- Hoskins, B. J., McIntyre, M., and Robertson, A. W.: On the use and significance of isentropic potential vorticity maps, *Quarterly Journal of the Royal Meteorological Society*, 111, 877–946, 1985.
- 530 Hsu, C. J. and Plumb, R. A.: Nonaxisymmetric thermally driven circulations and upper-tropospheric monsoon dynamics, *Journal of the atmospheric sciences*, 57, 1255–1276, 2000.
- Kosaka, Y., Nakamura, H., Watanabe, M., and Kimoto, M.: Analysis on the dynamics of a wave-like teleconnection pattern along the summertime Asian jet based on a reanalysis dataset and climate model simulations, *Journal of the Meteorological Society of Japan. Ser. II*, 87, 561–580, 2009.
- 535 Krishnamurti, T., Daggupati, S., Fein, J., Kanamitsu, M., and Lee, J. D.: Tibetan high and upper tropospheric tropical circulations during northern summer, *Bulletin of the American Meteorological Society*, 54, 1234–1250, 1973.
- Lee, J.-Y., Wang, B., Wheeler, M. C., Fu, X., Waliser, D. E., and Kang, I.-S.: Real-time multivariate indices for the boreal summer intraseasonal oscillation over the Asian summer monsoon region, *Climate Dynamics*, 40, 493–509, 2013.
- Liebmann, B. and Smith, C. A.: Description of a complete (interpolated) outgoing longwave radiation dataset, *Bull. Amer. Meteor. Soc.*, 77, 1275–1277, 1996.
- 540 Liu, Y., Hoskins, B., and Blackburn, M.: Impact of Tibetan orography and heating on the summer flow over Asia, *Journal of the Meteorological Society of Japan. Ser. II*, 85, 1–19, 2007.
- Luo, J., Pan, L. L., Honomichl, S. B., Bergman, J. W., Randel, W. J., Francis, G., Clerbaux, C., George, M., Liu, X., and Tian, W.: Space–time variability in UTLS chemical distribution in the Asian summer monsoon viewed by limb and nadir satellite sensors, *Atmospheric Chemistry and Physics*, 18, 12 511–12 530, <https://doi.org/10.5194/acp-18-12511-2018>, <https://www.atmos-chem-phys.net/18/12511/2018/>, 2018.
- 545 Nakamura, N.: Two-dimensional mixing, edge formation, and permeability diagnosed in an area coordinate, *Journal of the atmospheric sciences*, 53, 1524–1537, 1996.
- Nash, E. R., Newman, P. A., Rosenfield, J. E., and Schoeberl, M. R.: An objective determination of the polar vortex using Ertel’s potential vorticity, *Journal of Geophysical Research: Atmospheres*, 101, 9471–9478, 1996.
- 550 North, G. R., Bell, T. L., Cahalan, R. F., and Moeng, F. J.: Sampling errors in the estimation of empirical orthogonal functions, *Monthly Weather Review*, 110, 699–706, 1982.
- Norton, W. A.: Breaking Rossby waves in a model stratosphere diagnosed by a vortex-following coordinate system and a technique for advecting material contours, *Journal of the atmospheric sciences*, 51, 654–673, 1994.
- 555 Nützel, M., Dameris, M., and Garny, H.: Movement, drivers and bimodality of the South Asian High, *Atmospheric Chemistry and Physics*, 16, 14 755–14 774, 2016.
- Ortega, S., Webster, P. J., Toma, V., and Chang, H.-R.: Quasi-biweekly oscillations of the South Asian monsoon and its co-evolution in the upper and lower troposphere, *Climate Dynamics*, pp. 1–16, 2017.
- Ortega, S., Webster, P. J., Toma, V., and Chang, H. R.: The effect of potential vorticity fluxes on the circulation of the tropical upper troposphere, *Quarterly Journal of the Royal Meteorological Society*, 144, 848–860, <https://doi.org/10.1002/qj.3261>, 2018.
- 560 Pan, L., Kunz, A., Homeyer, C., Munchak, L., Kinnison, D., and Tilmes, S.: Commentary on using equivalent latitude in the upper troposphere and lower stratosphere, *Atmospheric Chemistry and Physics*, 12, 9187, 2012.

- Pan, L. L., Honomichl, S. B., Kinnison, D. E., Abalos, M., Randel, W. J., Bergman, J. W., and Bian, J.: Transport of chemical tracers from the boundary layer to stratosphere associated with the dynamics of the Asian summer monsoon, *Journal of Geophysical Research: Atmospheres*, 121, 2016.
- 565
- Park, M., Randel, W. J., Gettelman, A., Massie, S. T., and Jiang, J. H.: Transport above the Asian summer monsoon anticyclone inferred from Aura Microwave Limb Sounder tracers, *Journal of Geophysical Research: Atmospheres* (1984–2012), 112, 2007.
- Park, M., Randel, W. J., Emmons, L. K., Bernath, P. F., Walker, K. A., and Boone, C. D.: Chemical isolation in the Asian monsoon anticyclone observed in Atmospheric Chemistry Experiment (ACE-FTS) data, *Atmospheric Chemistry and Physics*, 8, 757–764, 2008.
- 570
- Park, M., Randel, W. J., Emmons, L. K., and Livesey, N. J.: Transport pathways of carbon monoxide in the Asian summer monsoon diagnosed from Model of Ozone and Related Tracers (MOZART), *Journal of Geophysical Research: Atmospheres* (1984–2012), 114, 2009.
- Ploeger, F., Gottschling, C., Griessbach, S., Groß, J.-U., Guenther, G., Konopka, P., Müller, R., Riese, M., Stroh, F., Tao, M., et al.: A potential vorticity-based determination of the transport barrier in the Asian summer monsoon anticyclone, *Atmospheric Chemistry and Physics*, 15, 13 145–13 159, 2015.
- 575
- Popovic, J. M. and Plumb, R. A.: Eddy shedding from the upper-tropospheric Asian monsoon anticyclone, *Journal of the Atmospheric Sciences*, 58, 93–104, 2001.
- Randel, W. J. and Park, M.: Deep convective influence on the Asian summer monsoon anticyclone and associated tracer variability observed with Atmospheric Infrared Sounder (AIRS), *Journal of Geophysical Research: Atmospheres* (1984–2012), 111, 2006.
- Randel, W. J., Park, M., Emmons, L., Kinnison, D., Bernath, P., Walker, K. A., Boone, C., and Pumphrey, H.: Asian monsoon transport of
- 580
- pollution to the stratosphere, *Science*, 328, 611–613, 2010.
- Santee, M., Manney, G., Livesey, N., Schwartz, M., Neu, J., and Read, W.: A comprehensive overview of the climatological composition of the Asian summer monsoon anticyclone based on 10 years of Aura Microwave Limb Sounder measurements, *Journal of Geophysical Research: Atmospheres*, 122, 5491–5514, 2017.
- Terao, T.: Barotropic disturbances on intraseasonal time scales observed in the midlatitudes over the Eurasian continent during the northern
- 585
- summer, *Journal of the Meteorological Society of Japan. Ser. II*, 76, 419–436, 1998.
- Vogel, B., Günther, G., Müller, R., Groß, J.-U., Hoor, P., Krämer, M., Müller, S., Zahn, A., and Riese, M.: Fast transport from Southeast Asia boundary layer sources to northern Europe: rapid uplift in typhoons and eastward eddy shedding of the Asian monsoon anticyclone, *Atmospheric Chemistry and Physics*, 14, 12 745–12 762, 2014.
- Vogel, B., Günther, G., Müller, R., Groß, J.-U., Afchine, A., Bozem, H., Hoor, P., Krämer, M., Müller, S., Riese, M., et al.: Long-range
- 590
- transport pathways of tropospheric source gases originating in Asia into the northern lower stratosphere during the Asian monsoon season 2012, *Atmospheric Chemistry and Physics*, 16, 15 301, 2016.
- Vogel, B., Müller, R., Günther, G., Spang, R., Hanumanthu, S., Li, D., Riese, M., and Stiller, G. P.: Lagrangian simulations of the transport of young air masses to the top of the Asian monsoon anticyclone and into the tropical pipe, *Atmospheric Chemistry and Physics*, 19, 6007–6034, <https://doi.org/10.5194/acp-19-6007-2019>, 2019.
- 595
- Wei, W., Zhang, R., Yang, S., Li, W., and Wen, M.: Quasi-Biweekly Oscillation of the South Asian High and Its Role in Connecting the Indian and East Asian Summer Rainfalls, *Geophysical Research Letters*, 46, 14 742–14 750, <https://doi.org/10.1029/2019GL086180>, 2019.
- Zhang, Q., Guoxiong, W., and Yongfu, Q.: The bimodality of the 100 hPa South Asia High and its relationship to the climate anomaly over East Asia in summer, *Journal of the Meteorological Society of Japan. Ser. II*, 80, 733–744, 2002.

	$\theta$	PV	domain	period
Randel and Park (2006)	360 K	0.93 PVU (1.5 PVU as MPV)	20–40° N 20–140° E	2003 May–Sep
Garny and Randel (2013)	360 K	0.3 PVU	15–45° N 0–180° E	2005–2009 May–Sep
Ploeger et al. (2015)	380 K	varies with time 2.6–4.4 PVU	10–60° N 10° W–160° E	2011–2013 20 Jun – 20 Aug
This study	360 K	0.5 PVU	10–50° N	1979–2016
	370 K	2.0 PVU	10° W–160° E	Jun–Aug
	380 K	3.5 PVU		

**Table 1.** Overview of the method of this study and previous studies which define the AMA based on the area enclosed by PV contours.

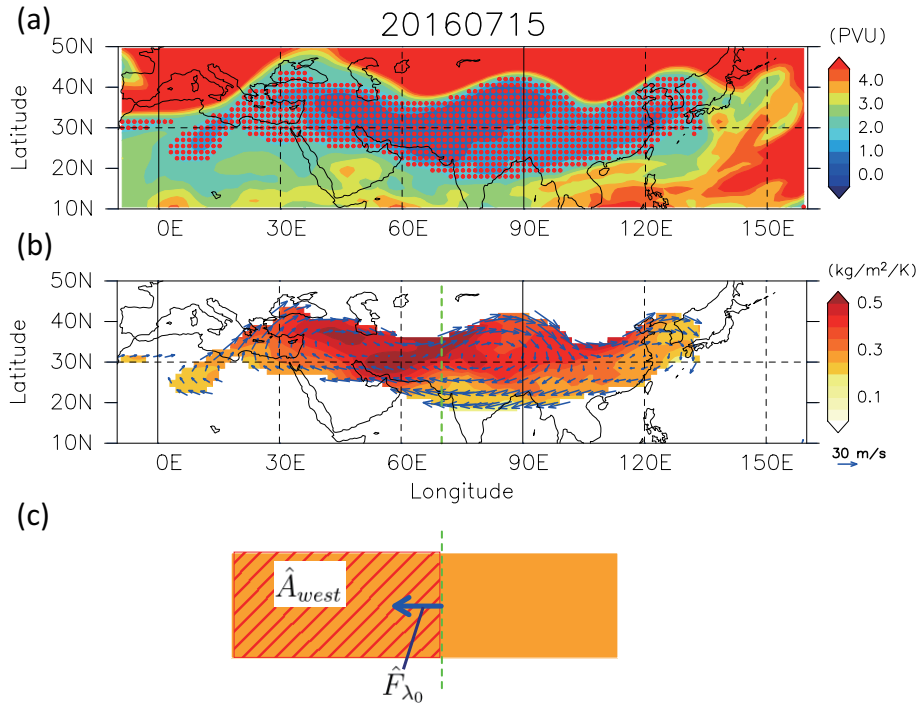


**Figure 1.** (a) Daily mean PV map at the 370 K isentropic level. The area of PV values below 2 PVU, defined as the area inside the AMA, is hatched by red dots. (b) Daily mean  $\sigma$  and horizontal wind. Values are shown only for the area inside the AMA. (c) A schematic description of  $\hat{A}_{west}$  and flux  $\hat{F}_{\lambda_0}$ . The reference longitude  $\lambda_0$  is set to 70° E in this example.

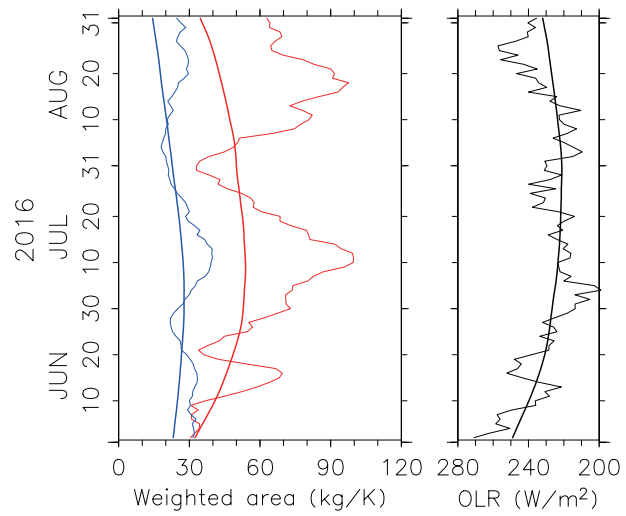


**Figure 2.** Daily thickness-weighted total low PV area defined at 360 K (red lines) and 370 K (blue lines), and the OLR averaged over 15° N – 30° N, 60° E–120° E, from June to August. Thin lines represent the daily data for 2016 and thick lines are for the 31-day filtered climatology.

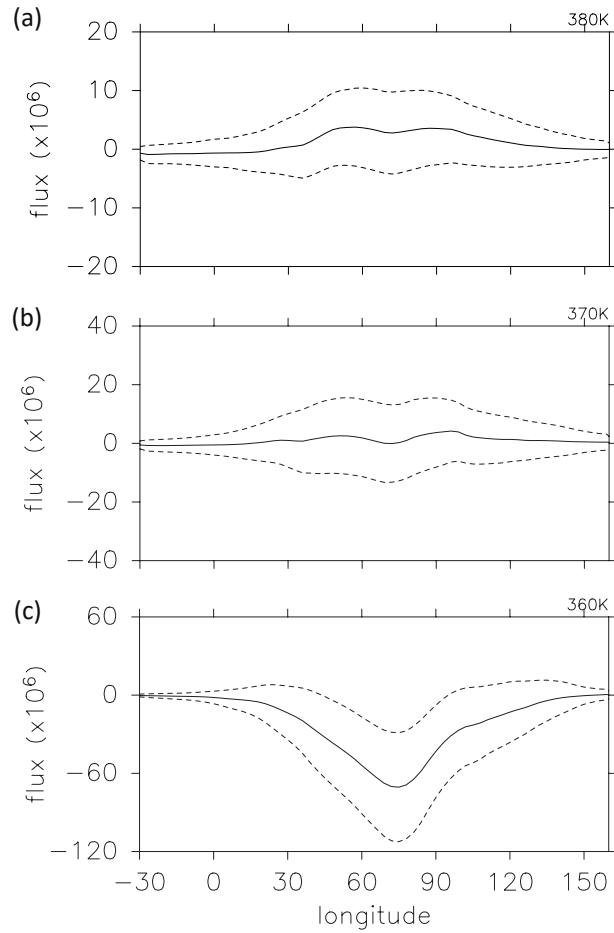


**Figure 3.** Climatological mean zonal flux of thickness-weighted low PV area as a function of longitude, calculated at the (a) 380 K, (b) 370 K, and (c) 360 K isentropic levels. The unit of the flux is  $\text{kg} \cdot \text{K}^{-1} \cdot \text{s}^{-1}$ . Solid and broken lines correspond to mean values and ranges of standard deviations.

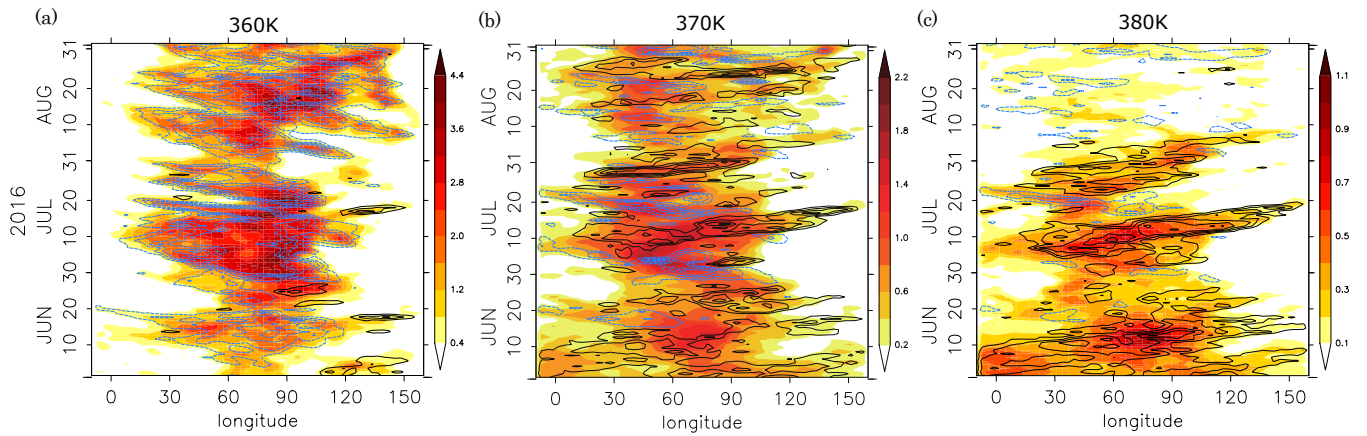


**Figure 4.** Time-longitude cross section of the air inside the AMA, defined based on the isentropic PV map [at the \(a\) 360 K, \(b\) 370 K, and \(c\) 380 K level](#). Color shadings show the thickness-weighted low PV area ( $\text{kg} \cdot \text{K}^{-1} 10^{12} \text{kg} \cdot \text{K}^{-1}$ ) [calculated for each longitude grid \(1.5 degree resolution\)](#). Black and blue contours respectively show the positive and negative zonal flux of thickness-weighted low PV area. The contour interval is  $1.5 \times 10^7 \text{ kg K}^{-1} \text{ s}^{-1}$  [4.0, 1.5, and  \$1.0 \times 10^7 \text{ kg K}^{-1} \text{ s}^{-1}\$  in \(a\), \(b\), and \(c\), respectively.](#)

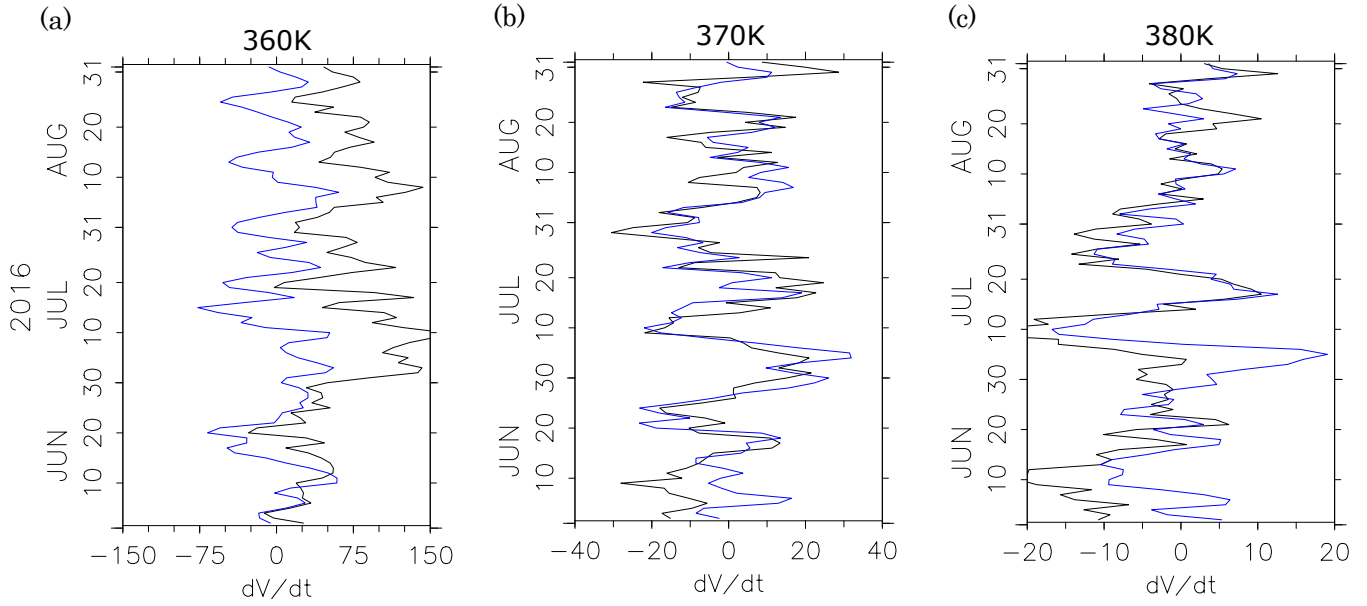


**Figure 5.** The tendency of the partial thickness-weighted anticyclone area  $\frac{d}{dt} \hat{A}_{\text{west}}$  (black: the left hand side of Eq. 6) and zonal flux  $\hat{F}$  at 60° E (blue: the first term on the right hand side) calculated at the (a) 360 K, (b) 370 K, and (c) 380 K level. The unit of the horizontal scale is  $10^6 \text{ kg} \cdot \text{K}^{-1} \text{ s}^{-1}$ .

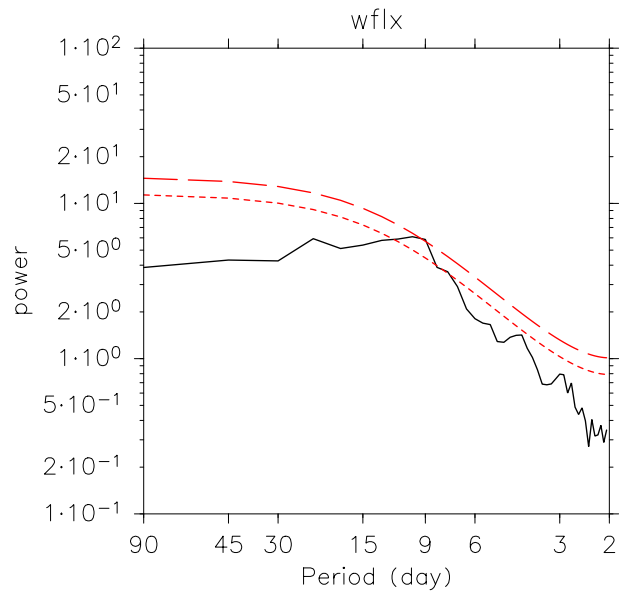


**Figure 6.** Power spectrum of the longitudinal flux of thickness-weighted low-PV area at  $60^\circ$  E [at the 370K level](#), calculated for June–August and averaged over 1979–2016. Broken red lines represent 95 and 99 confidence levels.

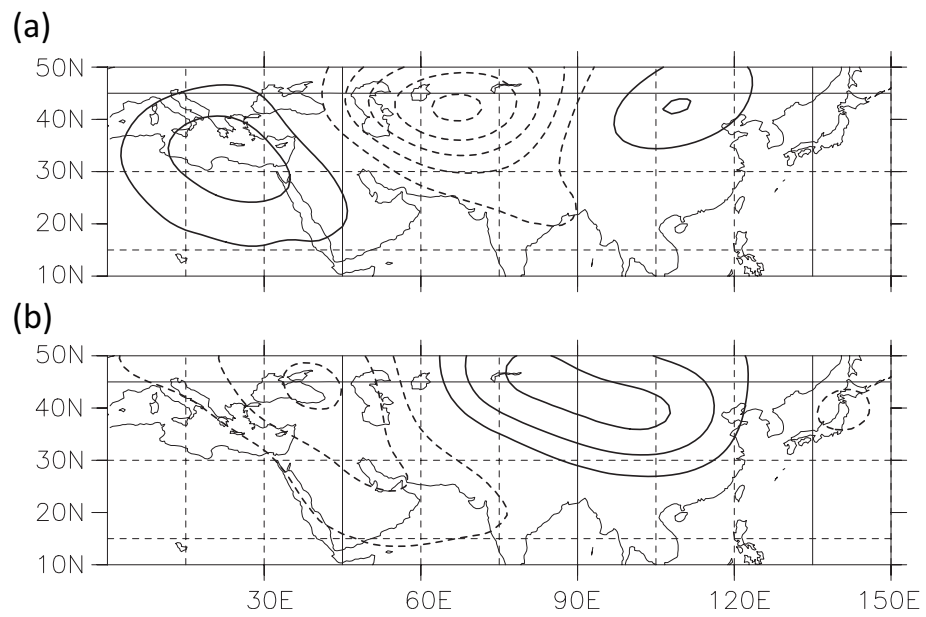


**Figure 7.** Spatial structure of (a) EOF 1 and (b) EOF 2 modes in geopotential height. The contour interval is 6 m. Zero contours are suppressed.

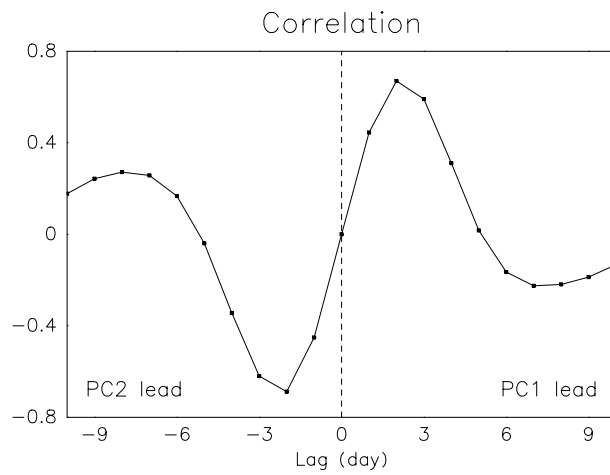


**Figure 8.** Lag-correlation in the unit of day between the principle component corresponding to the first and second EOF modes.

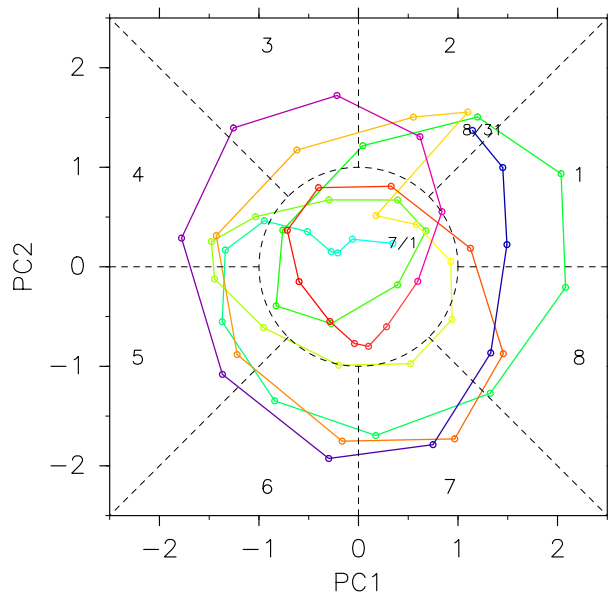


**Figure 9.** The spatial distribution of occurrence frequency definition of the air inside the anticyclone defined eight phases based on PV-value on 370-K isentropic level normalized two leading principal components. The daily phase progress in the year 2016 is shown for each of 8 phases example.

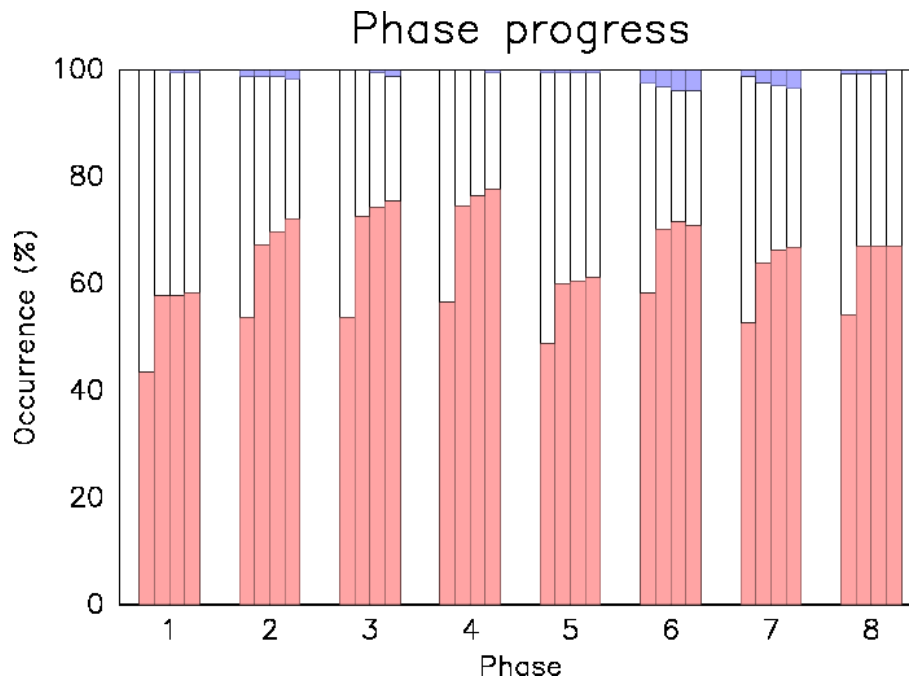


**Figure 10.** Percentage of forward (red) and backward (blue) phase progress starting from each phase. Four bars from left to right in each column correspond to time lags of 1 to 4 days.

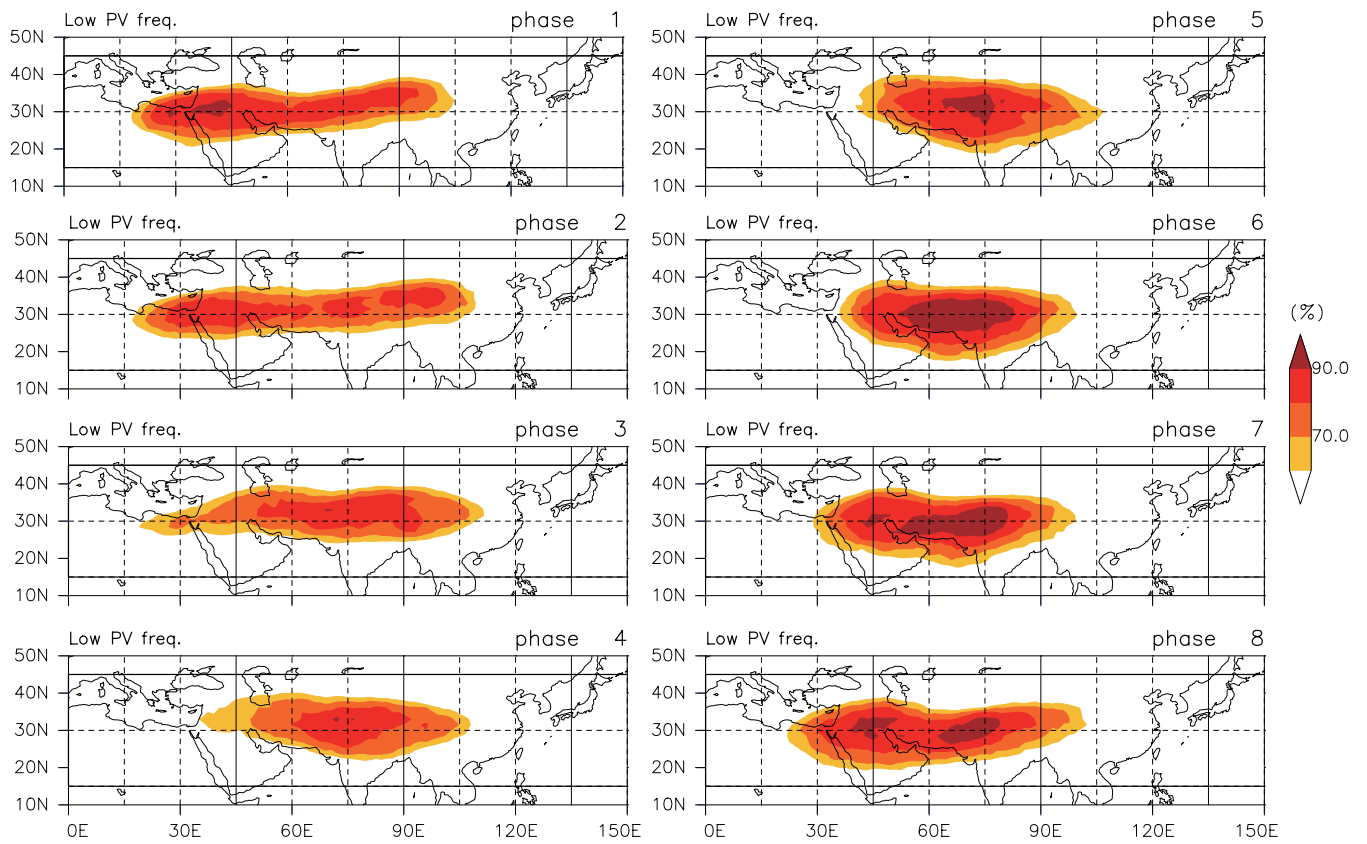


**Figure 11.** Percentage of PV value lower than the reference value of 2.0 PVU at the 370 K isentropic level for each phase.

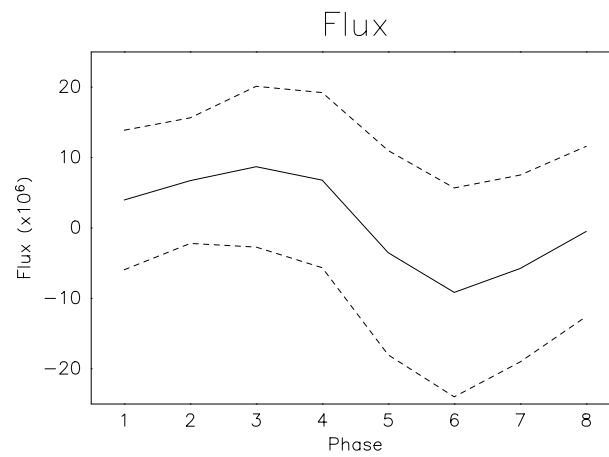


**Figure 12.** Mean value (solid line) and the range of standard deviation (broken lines) of the zonal flux of thickness-weighted low PV air ( $\text{Kg K}^{-1}\text{s}^{-1}$ ) at  $60^\circ \text{ E}$  calculated [at the 370 K level and](#) for each of 8 phases.

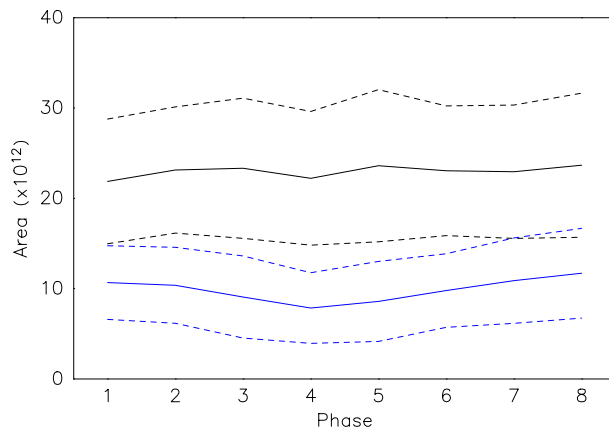


**Figure 13.** Mean values (solid lines) and the ranges of standard deviation (broken lines) of the area of thickness-weighted low PV air ( $\text{Kg K}^{-1}$ ) calculated at the 370 K level and for each of the 8 phases. Black and blue lines correspond to the total area and the partial area westward of  $60^\circ \text{E}$ , respectively.

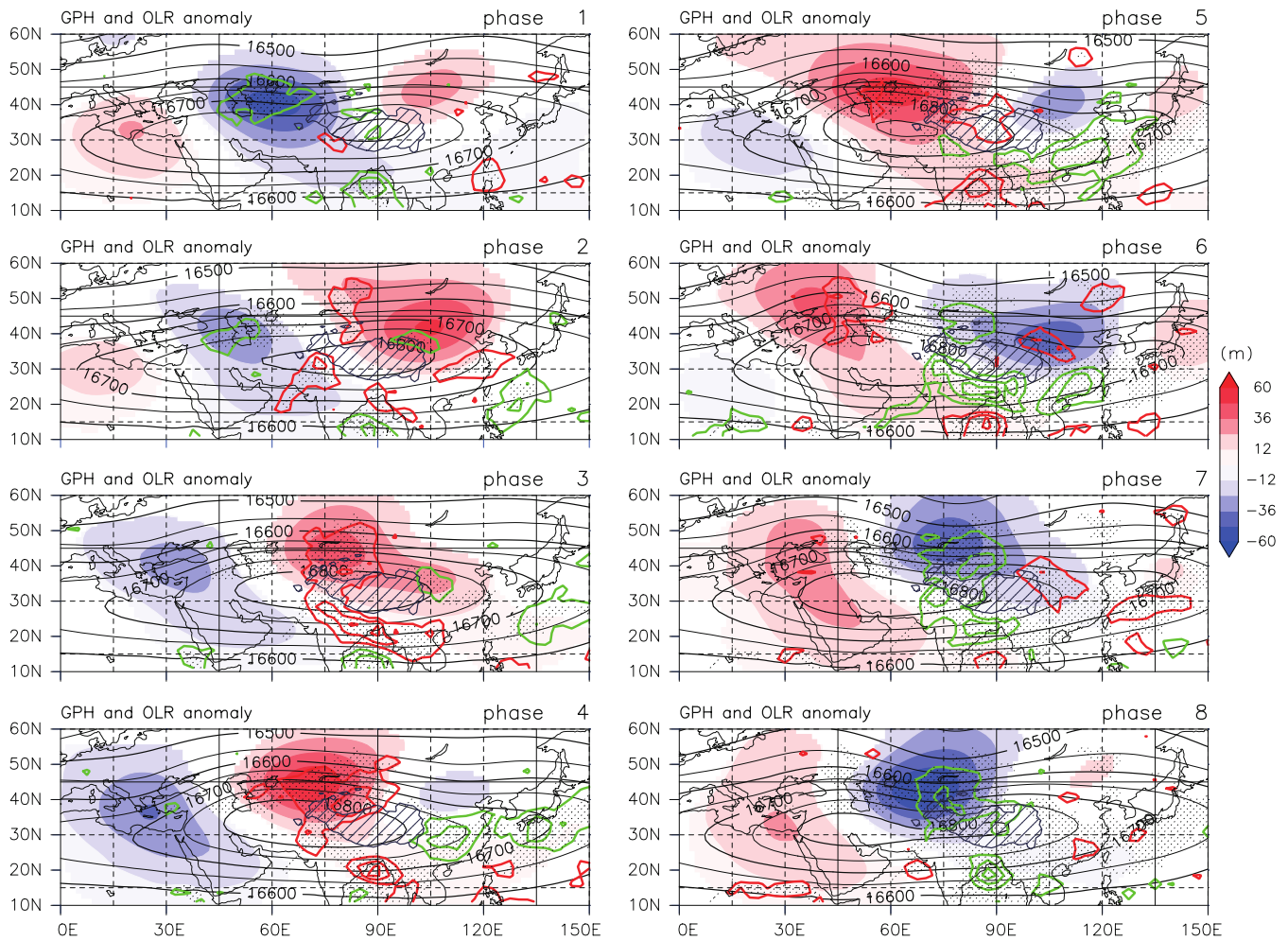


**Figure 14.** Composite mean maps of geopotential height [at 100 hPa level](#) (black contour) and its anomaly (shade), and the OLR anomaly (green and red contour) for each phase. Anomalies are calculated as deviations from climatology. The contour interval for geopotential height is 50 m. The contour interval for OLR anomaly is  $5 \text{ W m}^{-2}$ , with green and red contours respectively representing negative and positive anomalies. Shading of geopotential anomalies show only 95% significant areas by a standard  $t$ -test. The 95 % significant areas of OLR anomaly is hatched by dots. Areas with an elevation above 3000 m are hatched.

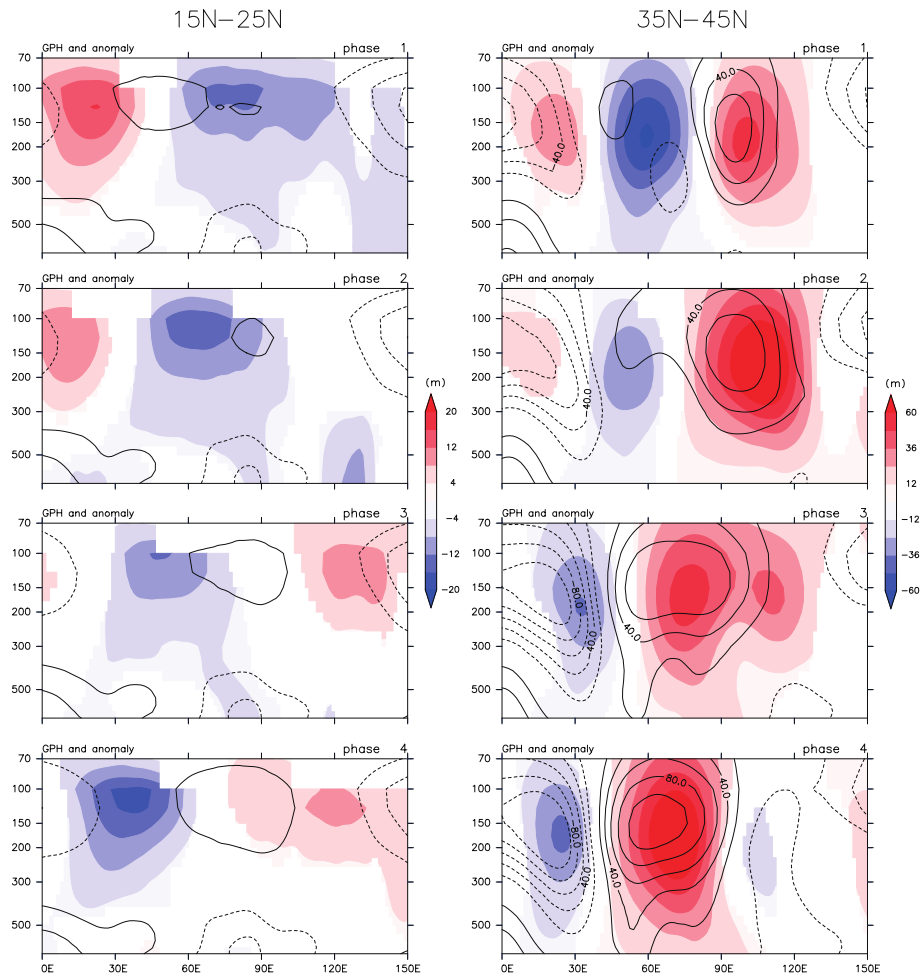


**Figure 15.** Composite mean of geopotential height in the longitude-pressure section. Contours show deviation from the zonal mean of the longitude sector, and its anomalies from climatology are shaded. The left and right columns respectively show maps averaged over  $15^{\circ}\text{E}$ – $25^{\circ}\text{E}$  and  $35^{\circ}\text{E}$ – $45^{\circ}\text{E}$ . Only the first four of eight phases are shown. The contour interval is 20 m. Only the 95% significant areas, determined by standard t-test, of geopotential anomalies are shaded. Note that different color scales are used for the left and right columns.

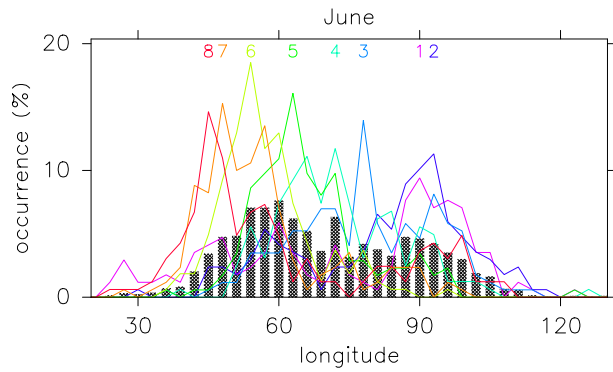


**Figure 16.** Longitudinal distribution of the occurrence frequency of the AMA center defined as the geopotential maximum at the 100 hPa pressure level. Hatched bars show the total average. Lines show partial averages of the data assigned for each phase, as denoted by numbers of the corresponding colors.

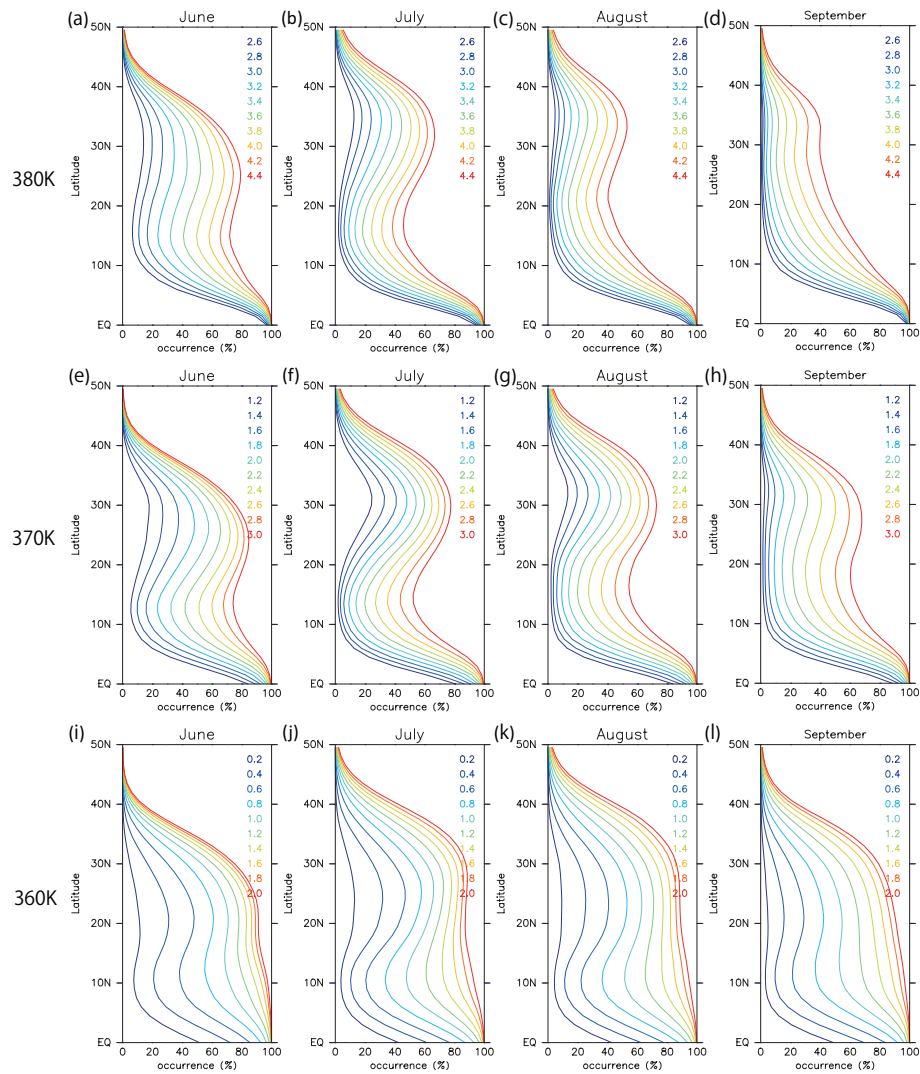


**Figure A1.** Percentage of the occurrence of grid points where PV is below the reference value between  $0^{\circ}$  E– $160^{\circ}$  E, as functions of latitude, calculated using ERA-Interim data from 1979 to 2016. Different line colors correspond to different reference PV values which are shown in the top-right of each figure.

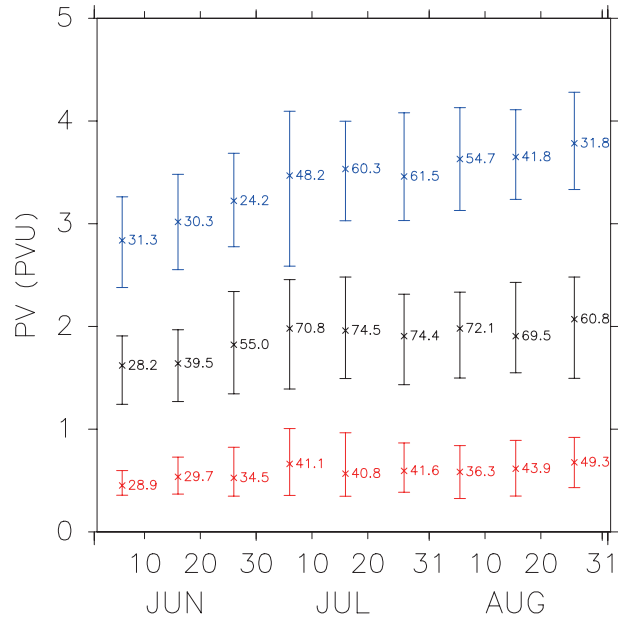


**Figure A2.** Statistics for the daily barrier PV values, determined objectively by the method of Ploeger et al. (2015), using ERA-Interim reanalysis data from 1979 to 2016. The horizontal axis is the time of year, with nine time ranges corresponding to the early, middle, and late periods of each month between June and August. Red, black and blue lines respectively show the results for 360, 370, and 380 K levels. Vertical lines show the range of PV values between 15th and 85th percentiles, with crosses in the middle corresponding to the median values. The numbers next to the crosses represent corresponding percentages of the cases when the barrier is successfully determined.

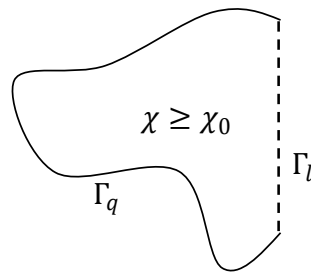


**Figure A3.** An example of the area enclosed by the isopleth of  $\chi$  and a specific longitude.  $\Gamma_q$  is the part of the isopleth  $\chi = \chi_0$ .  $\Gamma_l$  is the part of the circle of longitude  $\lambda = \lambda_0$ .